Icarus **140**, 379–407 (1999)
Article ID icar.1999.6130, available online at http://www.idealibrary.com on IDEAL®

Mainbelt Asteroids: Results of Arecibo and Goldstone Radar Observations of 37 Objects during 1980–1995

Christopher Magri

University of Maine at Farmington, 39 High Street—Preble Hall, Farmington, Maine 04938
E-mail: magri@maine.maine.edu

Steven J. Ostro, Keith D. Rosema, and Michael L. Thomas

MS 300-233, Jet Propulsion Laboratory, California Institute of Technology, Pasadena, California 91109-8099

David L. Mitchell

Space Sciences Laboratory, Centennial Drive at Grizzley Peak Blvd, University of California, Berkeley, California 94720

Donald B. Campbell

Department of Astronomy, Space Sciences Building, Cornell University, Ithaca, New York 14853-6801

John F. Chandler and Irwin I. Shapiro

Center for Astrophysics, 60 Garden Street, Cambridge, Massachusetts 02138

and

Jon D. Giorgini and Donald K. Yeomans

MS 301-150, Jet Propulsion Laboratory, California Institute of Technology, Pasadena, California 91109-8099

Received August 31, 1998; revised February 22, 1999

We report detailed results of Arecibo and Goldstone radar observations of 30 mainbelt asteroids (MBAs) during 1980–1995. In addition to estimates of radar cross section, radar albedo, and circular polarization ratio, we obtain new constraints on pole direction for several asteroids, with those for 21 Lutetia being particularly restrictive. We carry out statistical analyses of disk-integrated properties (radar albedo and polarization ratio) of all 37 radar-observed MBAs. M asteroids seem to have higher radar albedos and a wider range of albedos than do asteroids from the other taxonomic classes; there is no evidence that C and S MBAs have different albedo distributions; and there is some suggestion, worthy of future study, that primitive B, F, G, and P asteroids are not as radar-bright as C and S objects. There is no statistically significant evidence that different taxonomic classes have different polarization ratio distributions, despite suggestions to the contrary based on visual inspection of these distributions. The similarity between the C and S albedo distributions implies similar near-surface regolith bulk densities. The hypothesis of ordinary chondritic composition for the S-class asteroids is reasonably consistent with the radar data, provided that these asteroids have typical lunar porosities. Nevertheless, it is possible that some of these targets have high-porosity regoliths of stony-iron composition. Our M-class sample presumably contains both metallic objects (such as 216 Kleopatra and, probably, 16 Psyche) and less metallic objects.

Key Words: **asteroids; radar.**

1. INTRODUCTION

A goal of asteroid research is to attach physical significance to the asteroid taxonomic system (Tholen and Barucci 1989) and to relate mainbelt asteroids (MBAs) and near-Earth asteroids to meteorites that can be studied in detail on Earth. It has been recognized that MBAs have a wide range of radar properties, and there are good indications that at least some of this spread is related to taxonomic (mineralogical) differences within the MBA radar data set (Ostro *et al.* 1985; Mitchell *et al.* 1995, 1996). Thus, radar observations are a powerful source of otherwise unavailable information about MBA physical properties.

In 1980 a systematic program of MBA radar observations was begun at Arecibo. This program continued through 1992, just before the upgrading of the telescope began. Additionally, Goldstone observations of MBAs have been conducted since

0019-1035/99 $30.00

1990. A total of 37 MBAs was observed during 1980–1995; see Ostro (1998) for a tabulated history of asteroid radar detections and http://echo.jpl.nasa.gov/asteroids/index.html for an updated history.

Ostro *et al.* (1985) presented a summary of results for 20 MBAs. They reported that each asteroid appears much rougher than the Moon at some scale(s) between several meters and many kilometers. They also reported that the dispersion of MBA radar albedos implies substantial variations in surface porosity and/or metal concentration. Their highest albedo estimate, for 16 Psyche, is consistent with a metallic composition and lunar porosities. de Pater *et al.* (1994) carried out Goldstone–VLA aperture synthesis observations of four asteroids, obtaining novel constraints on the pole directions of MBAs 7 Iris and 324 Bamberga. Mitchell *et al.* (1995) presented detailed analyses of echoes from 7 Iris, 9 Metis, 12 Victoria, 216 Kleopatra, and 654 Zelinda, which show evidence for large-scale topography. They found that Kleopatra is a more reflective radar target than Psyche, making it the best mainbelt candidate for a metallic asteroid. Mitchell *et al.* (1996) presented detailed analyses of echoes from 1 Ceres, 2 Pallas, and 4 Vesta. They found that Pallas has a somewhat denser surface than Ceres and that both objects are much smoother than the Moon at decimeter scales but much rougher (rms slopes $> 20^\circ$) on larger scales, whereas Vesta is unusually rough at centimeter and decimeter scales.

Here we present detailed analyses of Arecibo and Goldstone observations not discussed by Mitchell *et al.* (1995, 1996); these experiments involve 30 asteroids. We then carry out statistical analyses of disk-integrated properties (radar albedo and polarization ratio) of all 37 radar-observed MBAs, searching for systematic trends. The next two sections describe our observations, which were similar for all the targets, and our analysis strategies, which were tailored for the strength of each target's echoes as well as for the nature of prior information about the target's dimensions and spin vector. To the degree possible, we have tabulated information about the observations, prior information, and analysis results. Section 4 is devoted to comments on various aspects of our investigations of individual targets, and Section 5 presents our statistical analyses of the entire MBA radar data set. Section 6 summarizes physical implications of our results.

2. OBSERVATIONS

Our observations used continuous-wave (cw) waveforms and yielded distributions of echo power vs Doppler frequency. These echo power spectra constitute one-dimensional images that can be thought of as scans of radar brightness taken through a slit that is kept parallel to the target's apparent spin vector and is moved across the target's disk.

Most of our observations used transmission of a circularly polarized wave and simultaneous reception of echoes in the same circular polarization as transmitted (the SC sense) and in the opposite circular polarization (OC). Techniques for data acquisition and reduction were nearly identical to those described by Ostro *et al.* (1992).

Observations of a target with roundtrip echo time delay RTT consisted of transmission for approximately RTT seconds followed by reception for a similar duration. Power spectra usually were obtained in real time and were blocked into groups each several minutes long. Reduction of data within each group produced a (nearly) background-removed OC/SC spectral pair in units of the rms noise. We tag each spectral pair with several dozen relevant quantities, including the rms noise expressed in units of radar cross section, the start/stop–receive epochs, the transmitter frequency, the spectral resolution, and radar telescope parameters (e.g., antenna gain, transmitter power, and system temperature). Table I lists observational parameters for our experiments.

3. ANALYSIS STRATEGIES AND USE OF PRIOR INFORMATION

3.1. Reference Ellipsoid Dimensions

We model all targets as triaxial ellipsoids with axis lengths $2a \geq 2b \geq 2c$. We use axis ratios a/b and b/c that have been estimated for some objects as a byproduct of the amplitude–magnitude pole determination method (Zappalà *et al.* 1984). Our primary source for such estimates is Magnusson's 1995 compilation of asteroid pole solutions (ftp://ftp.astro.uu.se/pub/Asteroids/SpinVectors/, henceforth Mag95). For the other targets, which have not been observed extensively enough to warrant such treatment, we estimate a/b from the published maximum lightcurve amplitude Δm:

$$\frac{a}{b} = 10^{0.4\Delta m}, \tag{1}$$

which holds for a geometrically scattering triaxial ellipsoid viewed from within the equatorial plane at zero solar phase angle (Gehrels 1970). In these cases we generally assume a prolate spheroid ($b/c = 1.0$) and assign standard errors to the axis ratios that we intend to be conservative. In particular, once we have chosen an error interval for a/b, we usually choose the interval for b/c by allowing the reference ellipsoid to be as flattened as it is elongated.

Radiometric diameters $D_{\rm IR}$—usually taken from Version 3.0 of *The IRAS Minor Planet Survey* (E. F. Tedesco 1997, http://pdssbn.astro.umd.edu/sbnhtml/asteroids/physical_param.html, henceforth Ted97)—have been published for most of our radar targets. For 19 Fortuna, 27 Euterpe, and 33 Polyhymnia, which were not observed by IRAS, we use TRIAD diameters (Bowell *et al.* 1979) and assign a 15% standard error that is intended to cover both estimation bias due to departures from a spherical shape (Brown 1985) and lower accuracy relative to IRAS data.

Our method for determining the axis lengths from $D_{\rm IR}$ and the axis ratios depends on whether or not an estimate for the asteroid's pole direction is available. The area of a triaxial ellipsoid from projection normal to the line of sight, i.e., the area as viewed

TABLE I
Observations[a]

Target	Observing dates (UT)	Obs.	Pol.	Runs	RA (h)	Dec (°)	Dist (AU)	Δf (Hz)
5 Astraea	1983 Feb 25, Mar 1–4	A	OC/SC	10	10.8 (0.09)	11 (1.0)	1.13 (0.004)	3
	1987 Feb 5–7	A	OC/SC	10	8.8 (0.03)	16 (0.3)	1.10 (0.002)	3
6 Hebe	1985 Jan 18–23	A	OC/SC	17	6.0 (0.05)	9 (0.9)	1.39 (0.041)	19
7 Iris	1995 Nov 23–25, 30, Dec 1–2	G	OC/SC	80	4.4 (0.15)	25 (1.2)	0.87 (0.006)	39
8 Flora	1981 Dec 4–5, 7–11	A	OC/SC	19	6.1 (0.12)	18 (0.4)	0.98 (0.010)	20
16 Psyche	1980 Nov 16–23	A	OC/SC	11[b]	5.2 (0.09)	18 (0.2)	1.70 (0.023)	20
	1985 Dec 7–11	A	OC/SC	10	4.8 (0.06)	18 (0.1)	1.69 (0.009)	19
18 Melpomene	1985 Dec 7–11	A	OC/SC	14	7.3 (0.05)	7 (0.1)	1.20 (0.015)	19
	1995 Sep 11, 17, 24, 26	G	OC/SC	39	23.6 (0.15)	−13 (3.5)	0.83 (0.003)	20
19 Fortuna	1982 Sep 29–Oct 3, Oct 5	A	OC/SC	12	1.4 (0.08)	10 (0.6)	1.08 (0.018)	19
	1986 Nov 23–24	A	OC/SC	4	3.7 (0.02)	18 (0.1)	1.10 (0.002)	10
20 Massalia	1987 Dec 2–7	A	OC/SC	21	4.5 (0.09)	21 (0.2)	1.12 (0.001)	5
21 Lutetia	1985 Oct 3–7	A	OC/SC	9	3.1 (0.03)	13 (0.1)	1.32 (0.021)	5
27 Euterpe	1986 Nov 20–24	A	OC/SC	13	2.4 (0.05)	12 (0.2)	1.08 (0.012)	10
33 Polyhymnia	1985 Oct 2, 4–6	A	OC/SC	10	1.7 (0.05)	11 (0.2)	0.99 (0.003)	5
41 Daphne	1985 Apr 26–28	A	OC/SC	9	13.1 (0.01)	7 (0.4)	1.10 (0.007)	19
	1985 Apr 25, 29–30	A	SL/OL	9	13.1 (0.03)	8 (0.9)	1.11 (0.018)	19
46 Hestia	1982 Nov 12–15	A	OC/SC	12	3.7 (0.05)	16 (0.2)	1.26 (0.002)	19
78 Diana	1990 Jan 11–16	A	OC/SC	16	8.4 (0.09)	29 (0.1)	1.12 (0.010)	5
80 Sappho	1983 Oct 26–31	A	OC/SC	16	2.2 (0.07)	15 (1.0)	0.91 (0.008)	10
84 Klio	1985 Oct 4–7	A	OC/SC	8	0.7 (0.05)	21 (0.0)	0.88 (0.003)	5
97 Klotho	1981 Jan 29–Feb 1	A	OC	6	8.1 (0.04)	8 (0.5)	1.23 (0.012)	10
	1993 Dec 30, 1994 Jan 3, 7, 9–10	G	OC/SC	54	7.3 (0.16)	4 (1.2)	1.12 (0.006)	20
105 Artemis	1988 Jun 10–11	A	OC/SC	6	16.8 (0.01)	16 (0.1)	1.07 (0.003)	4
139 Juewa	1983 Feb 26–Mar 4	A	OC/SC	11	9.8 (0.10)	24 (0.2)	1.37 (0.018)	7
144 Vibilia	1984 Oct 25–30	A	OC/SC	7	2.9 (0.07)	11 (0.1)	1.11 (0.003)	10
192 Nausikaa	1985 Oct 2, 4–5	A	OC/SC	7	23.7 (0.04)	4 (0.0)	0.83 (0.006)	5
194 Prokne	1990 Jul 30, Aug 1, 3	G	OC/SC	25	20.6 (0.05)	1 (1.0)	1.02 (0.007)	20
230 Athamantis	1985 Oct 2, 4, 6–7	A	OC/SC	6	22.6 (0.04)	7 (0.8)	1.34 (0.027)	5
324 Bamberga	1991 Sep 5–6, Oct 11–13	A	OC/SC	7	22.9 (0.47)	4 (3.2)	0.81 (0.066)	5
	1991 Sep 14	G	OC/SC	4	23.0 (0.00)	4 (0.0)	0.80 (0.000)	39
356 Liguria	1983 Oct 26–31	A	OC/SC	8	1.4 (0.08)	18 (0.1)	1.23 (0.002)	10
393 Lampetia	1986 Jul 16–18	A	OC/SC	12	19.8 (0.02)	11 (0.1)	0.92 (0.002)	3
	1986 Jul 19–20	A	SL/OL	10	19.8 (0.01)	11 (0.0)	0.91 (0.001)	3
532 Herculina	1987 Apr 4, 6–8	A	OC/SC	10	13.1 (0.05)	23 (0.3)	1.37 (0.008)	19
554 Peraga	1984 Oct 25–30	A	OC/SC	16	0.8 (0.06)	11 (0.5)	1.11 (0.015)	10
694 Ekard	1983 Oct 26–31	A	OC/SC	16	0.1 (0.01)	17 (1.5)	1.00 (0.032)	10
796 Sarita	1991 Oct 11–13	A	OC	11	3.0 (0.03)	16 (0.4)	0.91 (0.005)	5

[a] Transmitter frequency is 2380 MHz for Arecibo (A) and 8510 MHz for Goldstone (G) (except for 194 Prokne, for which it is 8495 MHz). For each experiment we give received polarization(s); the number of transmit-receive cycles, or runs; right ascension, declination, and distance from Earth for epochs near the weighted midpoint of observation (with the range of values spanned in parentheses); and the raw frequency resolution Δf.

[b] This experiment included 11 runs in which only OC echoes were received, and 5 runs in which only SC echoes were received.

at subobserver latitude δ and rotational phase ϕ, is

$$A_{\text{proj}} = \pi ab\left\{\sin^2\delta + \left(\frac{c}{b}\right)^2\cos^2\delta - \left[1-\left(\frac{b}{a}\right)^2\right]\left(\frac{c}{b}\right)^2\cos^2\delta\sin^2\phi\right\}^{\frac{1}{2}}, \quad (2)$$

where $\phi = 0°, 180°$ corresponds to the maximum-breadth orientations. We can define an area factor ζ such that this projected area of the model ellipsoid, averaged over all observations, is equal to $\zeta\pi ab$. (Note that $c/a \le \zeta \le 1$.) When the pole direction—and hence δ—is known (and is nearly constant, which is the usual case), the expectation value of ζ is $1/\pi ab$ times the mean of Eq. (2) over all ϕ:

$$\langle\zeta\rangle = \frac{2}{\pi}E(k)\sqrt{\sin^2\delta + \left(\frac{c}{b}\right)^2\cos^2\delta}. \quad (3)$$

Here $E(k)$ is the complete elliptic integral of the second kind,

$$E(k) = \int_0^{\frac{\pi}{2}}\sqrt{1-k^2\sin^2\theta}\,d\theta \quad (4)$$

TABLE II
Prior Information

Target	Class[a]	D_{IR}[b]	Pole direction[c] λ	Ref.	β	Ref.	δ_{IR}[d]	P[e]	Ellipsoid diameters[f]	Obs'n Year[g]	δ_{rad}[h]	$\langle A_{proj}\rangle$[i]	D_{eff}[j]	$B_{max}(\delta_{rad}=0)$[k]
5 Astraea	S	119 ± 12 (6.5)	123 ± 10	(1)	+51 ± 10	(1)	−31 ± 10	16.801	143 × 115 × 100 ± 12%	1983	−34 ± 10	11400 ± 2600	120 ± 14	236 ± 27
										1987	−37 ± 10	11400 ± 2600	120 ± 14	”
6 Hebe	S	185 ± 10 (2.9)	358 ± 10	(1)	+40 ± 20	(2)	−10 ± 10	7.274	213 × 187 × 170 ± 8%	1985	+10 ± 10	26900 ± 3000	185 ± 10	811 ± 61
7 Iris	S	200 ± 20 (10.0)	15 ± 5	(3)	+25 ± 15	(3)	+19 ± 8	7.139	260 × 220 × 155 ± 15%	1995	−34 ± 8	34900 ± 7400	211 ± 22	3610 ± 550
8 Flora	S	136 ± 7 (2.3)	140 ± 10	(2)	+30 ± 20	(2)	−10 ± 10	12.8	156 × 142 × 124 ± 10%	1981	−30 ± 15	14900 ± 1900	138 ± 9	338 ± 36
16 Psyche	M	253 ± 25 (4.0)	35 ± 10	(1)	−21 ± 10	(1)	+69 ± 10	4.196	294 × 226 × 174 ± 11%	1980	−45 ± 10	44300 ± 9400	237 ± 25	1940 ± 210
										1985	−50 ± 10	45800 ± 9700	241 ± 26	”
18 Melpomene	S	141 ± 14 (2.8)	0 ± 30	(4)	0 ± 15	(4)	+56 ± 20	11.57	169 × 121 × 121 ± 13%	1985	+19 ± 30	14000 ± 4700	134 ± 22	404 ± 52
										1995 G	−78 ± 25	15700 ± 3200	141 ± 14	1450 ± 190
19 Fortuna	G	226 ± 34 (—)	79 ± 10	(1)	+51 ± 10	(1)	—	7.443	255 × 206 × 206 ± 18%	1982	−21 ± 10	38900 ± 14200	223 ± 41	951 ± 175
										1986	−35 ± 10	38900 ± 14200	223 ± 41	”
20 Massalia	S	146 ± 15 (9.3)	28 ± 10	(1)	+74 ± 10	(1)	−16 ± 10	8.098	166 × 138 × 138 ± 17%	1987	−11 ± 10	16600 ± 3800	145 ± 17	567 ± 95
21 Lutetia	M	96 ± 10 (4.1)	228 ± 14	(5)	+29 ± 19	(5)	+7 ± 11	8.16	123 × 94 × 82 ± 14%	1985	+65 ± 19	8700 ± 2200	105 ± 13	416 ± 56
27 Euterpe	S	118 ± 18 (—)	—				—	8.5	127 × 110 × 85 ± 20%	1986	—	10900 ± 3900	118 ± 21	414 ± 87
33 Polyhymnia	S	62 ± 9 (—)	—				—	18.60	68 × 59 × 59 ± 19%	1985	—	3000 ± 1100	62 ± 11	101 ± 19
41 Daphne	C	174 ± 17 (11.7)	342 ± 10	(1)	−34 ± 10	(1)	+5 ± 10	5.988	221 × 170 × 155 ± 13%	1985	+55 ± 10	27400 ± 6300	187 ± 21	1020 ± 130
46 Hestia	P	124 ± 6 (3.6)	—				—	21.7	133 × 121 × 121 ± 11%	1982	—	12100 ± 1800	124 ± 9	170 ± 19
78 Diana	C	121 ± 6 (2.7)	33 ± 20	(6)	+13 ± 20	(6)	+8 ± 20	7.23	131 × 116 × 116 ± 17%	1990	−4 ± 20	11400 ± 1200	120 ± 6	504 ± 87
80 Sappho	S	78 ± 10 (1.7)	46 ± 15	(7)	+10 ± 15	(7)	−75 ± 15	14.03	93 × 68 × 36 ± 15%	1983	−76 ± 15	4900 ± 1300	79 ± 10	183 ± 28
84 Klio	G	79 ± 8 (1.6)	—				—	—	79 × 79 × 79 ± 27%	1985	—	4900 ± 1600	79 ± 13	see Appendix
97 Klotho	M	83 ± 8 (4.5)	—				—	35.0	98 × 75 × 75 ± 18%	1981	—	5400 ± 1300	83 ± 10	77 ± 14
										1993–4 G	—	5400 ± 1100	83 ± 8	277 ± 50
105 Artemis	C	119 ± 12 (2.8)	—				—	17.	135 × 112 × 112 ± 18%	1988	—	11100 ± 3200	119 ± 17	219 ± 55
139 Juewa	CP	157 ± 16 (2.8)	117 ± 25	(8)	+50 ± 25	(8)	−36 ± 25	20.9 or 41.8	202 × 158 × 99 ± 20%	1983	−46 ± 25	21200 ± 5800	164 ± 22	268 ± 53 or 134 ± 27
144 Vibilia	C	142 ± 7 (2.9)	—				—	13.81	153 × 136 × 136 ± 13%	1984	—	15800 ± 2800	142 ± 13	307 ± 40
192 Nausikaa	S[l]	103 ± 10 (1.9)	320 ± 20	(2)	−45 ± 15	(2)	+46 ± 15	13.62	131 × 97 × 65 ± 14%	1985	−29 ± 15	7100 ± 1900	95 ± 13	267 ± 38
194 Prokne	C	168 ± 17 (4.1)	—				—	15.67	199 × 153 × 153 ± 20%	1990 G	—	22300 ± 5400	169 ± 20	1260 ± 250
230 Athamantis	S	109 ± 11 (2.0)	—				—	24.0	117 × 105 × 105 ± 17%	1985	—	9300 ± 2400	109 ± 14	135 ± 23
324 Bamberga	CP	229 ± 11 (7.4)	—				+13 ± 30[m]	29.41	239 × 227 × 227 ± 7%	1991	0 ± 30[m]	41300 ± 4500	229 ± 12	225 ± 15
										1991 G	”	”	”	804 ± 55
356 Liguria	C	131 ± 13 (2.6)	—				—	31.82	148 × 124 × 124 ± 17%	1983	—	13500 ± 3000	131 ± 15	129 ± 22
393 Lampetia	C	97 ± 31 (31.4)	—				—	38.7 or 19.35	97 × 97 × 97 ± 32%	1986	—	7400 ± 4800	97 ± 31	69 ± 22 or 139 ± 44
532 Herculina	S	222 ± 22 (7.6)	290 ± 10	(9)	+30 ± 15	(9)	−60 ± 20	9.405	244 × 204 × 185 ± 14%	1987	−3 ± 10	33700 ± 8000	207 ± 25	720 ± 97
554 Peraga	FC	96 ± 10 (4.1)	—				—	13.63	108 × 90 × 90 ± 18%	1984	—	7200 ± 1900	96 ± 13	220 ± 40
694 Ekard	CP:	91 ± 12 (4.0)	96 ± 10	(1)	+31 ± 10	(1)	−4 ± 10	5.922	135 × 97 × 69 ± 17%	1983	−9 ± 10	6500 ± 1800	91 ± 13	633 ± 105
796 Sarita	XD[n]	45 ± 5 (1.5)	—				—	7.75	53 × 41 × 41 ± 20%	1991	—	1590 ± 420	45 ± 6	188 ± 37

[a] Taxonomic classification (Tholen 1989) based on visual and infrared data.

[b] Radiometric diameter (km), based on IRAS data (Ted97) when available, or, for 19 Fortuna, 27 Euterpe, and 33 Polyhymnia, taken from the TRIAD compilation (Bowell *et al.* 1979). These diameters assume a spherical asteroid that obeys the Standard Thermal Model (Lebofsky and Spencer 1989). Formal uncertainties derived by Ted97 on this assumption are given in parentheses. Departures from sphericity may bias diameter estimates to an extent that depends on the asteroid's shape and its orientation at the time of the infrared observations (Brown 1985). Our adopted standard errors have been increased accordingly.

[c] Ecliptic coordinates (deg) of the spin vector. Most of our targets have ambiguous pole solutions; we have listed only one possible pole direction per target, as others predict similar viewing geometries for IRAS and radar observations. References listed in parentheses: (1) consensus ("synthesis") value from Mag95, with 10° standard error assumed; (2) Mag95 lists several published pole solutions but no consensus value, so we have formulated an estimate whose one-standard deviation range encompasses the individual published estimates; (3) Mitchell *et al.* (1995); (4) Hoffmann and Geyer (1990); (5) same as (2), but with solution from Michałowski (1996) considered in addition to earlier estimates compiled by Mag95; (6) Harris and Young (1989); (7) Michałowski (1993), but with standard error increased from 6° to 15°; (8) Michałowski (1993), but with standard error increased from roughly 13° to 25°; (9) same as (2), but with solutions from Michałowski *et al.* (1995) and Michałowski (1996) considered in addition to earlier estimates compiled by Mag95.

[d] SubIRAS latitude (deg) over the duration of IRAS observations, based on photometric pole estimates (see footnote *c*).

[e] Sidereal rotation period (h), taken from Lagerkvist *et al.* (1996) and references therein.

[f] Adopted axis dimensions (km) based on a combination of radiometric, lightcurve, and occultation data (see text). The stated percentage standard error refers to the largest diameter $2a$.

[g] Year of radar observation. Goldstone observations are identified by a G.

[h] Subradar latitude (deg) over the duration of radar observations, based on photometric pole estimates (see footnote *c*).

[i] Mean projected area (km^2) of the reference ellipsoid as viewed by the radar. This is an unweighted mean over all rotation phases. The stated standard error incorporates uncertainties in the axis lengths, differences between IRAS and radar viewing geometries, and the rotational phase coverage for the IRAS and radar data.

[j] Effective diameter (km) of the target. By definition, the mean projected area of the reference ellipsoid as viewed by the radar is equal to $\pi D_{\mathrm{eff}}^2/4$. Standard errors propagate from those stated for $\langle A_{\mathrm{proj}} \rangle$.

[k] Maximum-breadth echo bandwidth (Hz) predicted by the reference ellipsoid for a spectral sum obtained with an equatorial view and complete rotational phase coverage. Standard errors propagate from those stated for diameter $2a$; for 8 Flora, 27 Euterpe, and 105 Artemis, significant uncertainties in P have also been factored in.

[l] 192 Nausikaa's taxonomic class is S on the Tholen system (Tholen 1989), and recently was revised from V0 to S1 according to the G-mode classification (Birlan *et al.* 1996).

[m] SubIRAS and subradar latitudes stated for 324 Bamberga are based on the analysis of monostatic and bistatic radar data by de Pater *et al.* (1994).

[n] We follow Rivkin *et al.* (1995) and Belskaya and Lagerkvist (1996) in treating 796 Sarita as an M-class object rather than as a P or D-class object, based on its moderately high visual albedo $p_{\mathrm{V}} = 0.197 \pm 0.013$.

whose modulus k is given by

$$k = \sqrt{\frac{1 - \left(\frac{b}{a}\right)^2}{\left(\frac{b}{c}\right)^2 \tan^2\delta + 1}} \quad (5)$$

If we know the subobserver latitudes of IRAS and radar observations (δ_{IR} and δ_{rad}), we can insert them into Eq. (3) to compute area factors ζ_{IR} and ζ_{rad}. We can then use the model axis ratios and the IRAS diameter D_{IR} to estimate the lengths of the principal axes of our reference ellipsoid. Setting $\pi D_{IR}^2/4 = \zeta_{IR}\pi ab = \zeta_{IR}\pi a^2(b/a)$, we obtain the diameter of the longest principal axis

$$2a = D_{max} = D_{IR}\sqrt{\frac{\left(\frac{a}{b}\right)}{\zeta_{IR}}} \quad (6)$$

from which we can then obtain $2b$ and $2c$. The two area factors can also be used to find the mean projected area viewed by the radar:

$$\langle A_{proj}\rangle = \frac{\zeta_{rad}}{\zeta_{IR}}\frac{\pi}{4}D_{IR}^2. \quad (7)$$

For elongated asteroids, incomplete IRAS or radar rotational phase coverage will increase the uncertainties (here and hereafter meaning "standard errors") associated with these estimates. If, for example, only two IRAS sightings were made and the target happened to be prolate and viewed nearly end-on both times, we would underestimate the axis lengths and $\langle A_{proj}\rangle$. The opposite problem (all sightings at maximum-breadth orientations) is equally likely. We therefore assume that incomplete phase coverage increases the variances of our estimators without biasing them.

The main hindrance in determining radar phase coverage for a given opposition is the lack of absolute phase information; that is, none of the targets discussed here shows unambiguous bandwidth variations which would allow us to define an epoch at which $\phi = 0^\circ$. IRAS observations involve several brief sightings spaced weeks or months apart, so phase coverage is difficult to assess. Hence we simply use the number of sightings as a guide to making subjective estimates of the quality of IRAS' phase coverage.

The pole directions of 13 of our targets are unknown. In these cases we estimate the area factor ζ_{IR} by assuming that all viewing geometries are equally likely; that is, we numerically average Eq. (2) over all ϕ and $\cos\delta_{IR}$, and divide by πab. We can then use Eq. (6) to compute axis lengths as before, but with larger uncertainties which now depend on the degree of flattening. In the absence of pole information we assume that IRAS and the radar viewed the same projected area: $\langle A_{proj}\rangle = \pi D_{IR}^2/4$. Such estimates are again more uncertain for flattened asteroids, except in cases where IRAS and the radar viewed the target at similar orientations or at antipodal ones.

We can combine the estimated axis lengths with the rotation period P to estimate $B_{max}(\delta_{rad} = 0)$, the predicted echo bandwidth when the target is viewed from within the equatorial plane and is oriented with its maximum breadth D_{max} normal to the line of sight:

$$B_{max}(\delta_{rad} = 0) = \frac{4\pi D_{max}}{\lambda P}. \quad (8)$$

For a sum of noise-free spectra obtained at all rotation phases, the corresponding bandwidth B would equal $B_{max}(\delta_{rad} = 0)\cos\delta_{rad}$.

Prior information for all of our radar targets is listed in Table II.

3.2. Radar Properties

Almost all radar data considered in this paper are Doppler spectra simultaneously received in orthogonal (OC and SC) circular polarizations. Single scattering from large, smooth "facets" gives a purely OC echo. Processes which can produce both SC and OC echo power include single scattering from wavelength-scale near-surface structure and multiple scattering of all sorts.

We estimate bandwidth B from the innermost zero-crossings of spectra which have been formed, first, by summing all data together, and second, by averaging the positive- and negative-frequency halves of these sums. Such "folded" spectra have $\sqrt{2}$ higher signal-to-noise ratios (SNRs). We then smooth the folded sum to an appropriate effective frequency resolution. Wishing to smooth just enough to minimize the influence of random baseline noise on our estimate, we compute zero-crossing bandwidth B_{ZC} for several frequency resolutions. These values of B_{ZC} sometimes exhibit large fluctuations at fine resolutions, but they become more stable, and increase slowly and steadily at coarser resolutions. In such cases, stated estimates $\hat{B}_{ZC}$ refer to a resolution at the boundary between these two regimes; otherwise we use the raw resolution to obtain $\hat{B}_{ZC}$. Uncertainties are subjectively determined by inspecting the fluctuations in B_{ZC} near the chosen resolution.

An alternative, more sophisticated method for estimating B would be to fit a model spectrum to the data, based on an assumed parametric form for the target's shape and angular scattering law (e.g., Mitchell *et al.* 1995, 1996). Yet the asteroids discussed here have radar data sets that are too weak, or else axis lengths that are too imprecisely known, for such fits to yield meaningful results. Hence we rely on the subjective method outlined above. The agreement between our radar-based shape models of near-Earth asteroid 433 Eros (Ostro *et al.* 1990, Mitchell *et al.* 1998) and the model based on spacecraft images (see http://near.jhuapl.edu/iod/19990201/index.html) gives us confidence that our bandwidth and uncertainty estimates are realistic.

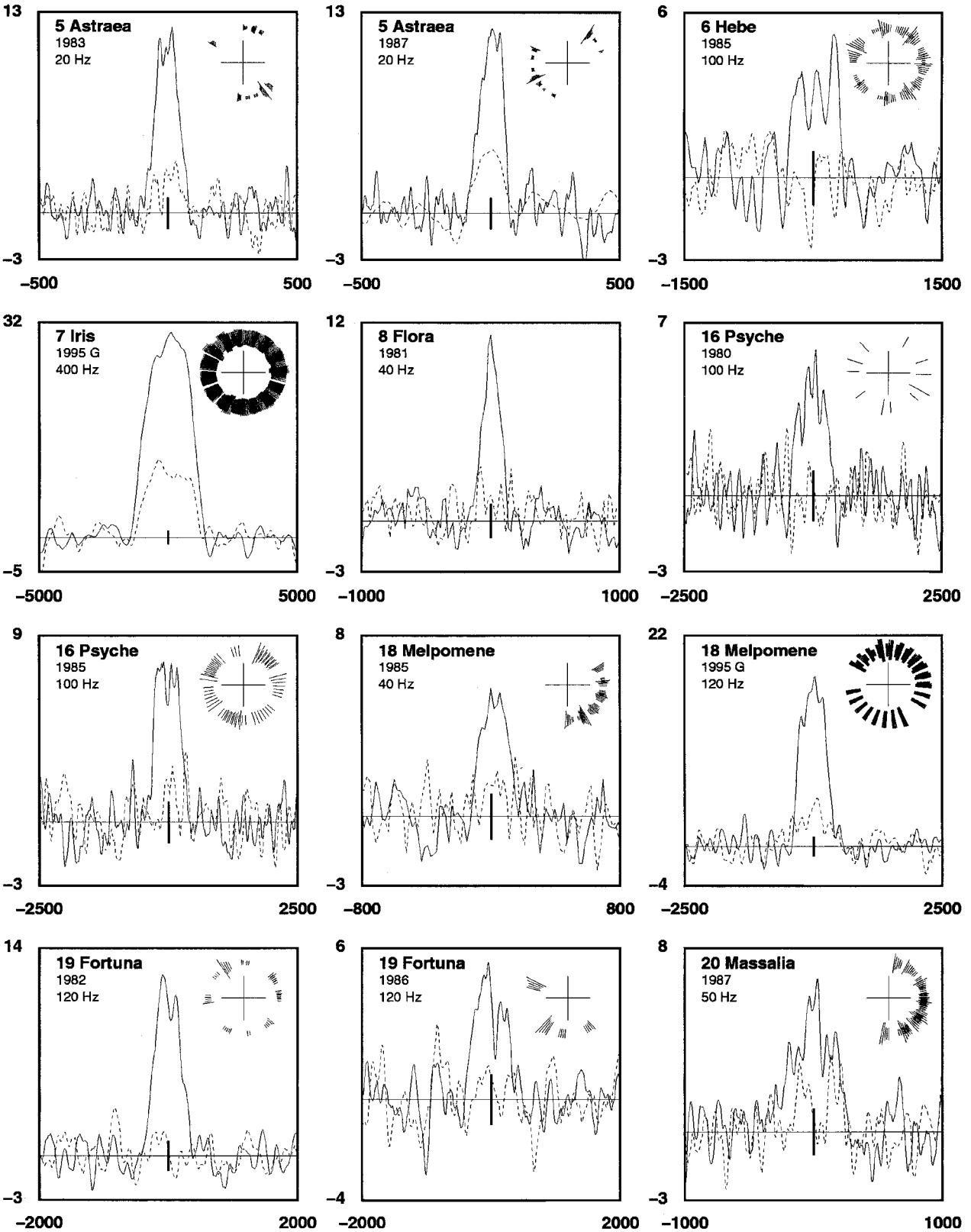

FIG. 1. Weighted sums of OC (solid lines) and SC (dashed lines) echo spectra for all 36 circular-polarization radar experiments. Echo power, in units of standard deviations of the noise, is plotted versus Doppler frequency (Hz) relative to that of hypothetical echoes from the target's center of mass. The vertical bar at the origin indicates ± 1 standard deviation of the OC noise. Each label gives the target name, the observation year (with Goldstone experiments denoted by G), and the frequency resolution of the displayed data. Rotation phase coverage is depicted in the upper right portion of each plot for which these data are available in computer-readable format. Each radial line segment denotes the phase (relative to an arbitrary epoch) of an independent spectrum formed by summing a several-minute data "group" (see Section 2); the length of the segment is proportional to the OC noise standard deviation of the corresponding spectrum. There is no phase correspondence from year to year for targets observed more than once.

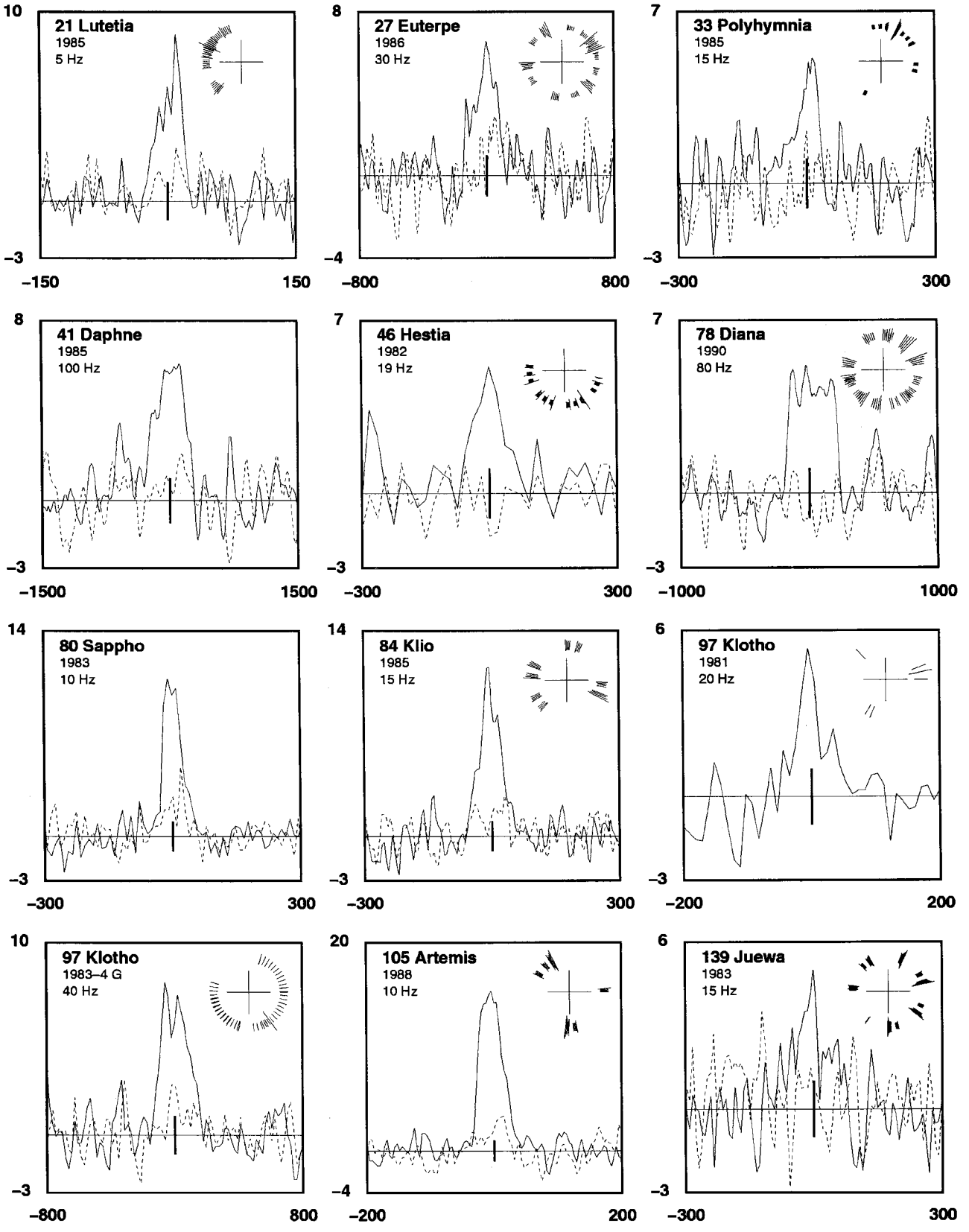

FIG. 1—*Continued*

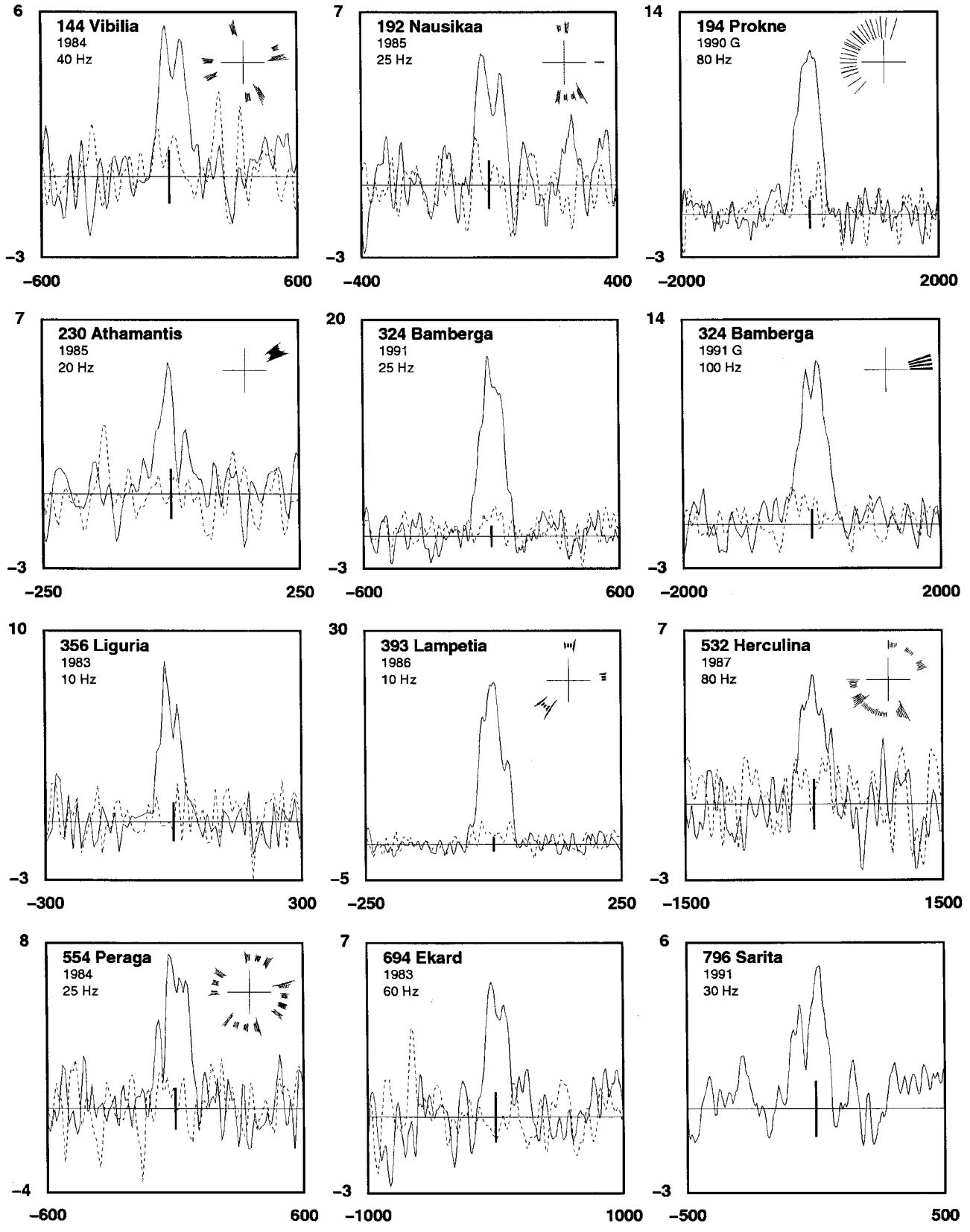

FIG. 1—*Continued*

Another bandwidth estimator is based on the equivalent bandwidth B_{eq}, defined as

$$B_{eq} = \frac{\left(\int S(f)\,df\right)^2}{\int S^2(f)\,df} \Rightarrow \frac{\left(\sum_i S_i\right)^2}{\sum_i (S_i)^2}\Delta f, \qquad (9)$$

where Δf is the frequency channel width and S_i is the signal in the ith channel (Tiuri 1964). A rectangular spectrum has $B_{eq} = B$, while any other spectral shape yields $B_{eq} < B$ in the absence of noise. Hence B_{eq} serves as a conservative lower limit on B. We find that B_{eq} is much less sensitive than B_{ZC} to frequency smoothing. We obtain estimates $\hat{B}_{eq}$ in the manner described above for $\hat{B}_{ZC}$, except that we use unfolded spectra.

Integration of "raw" (unsmoothed and unfolded) OC and SC spectra yields the radar cross sections σ_{OC} and σ_{SC}. The radar cross section of a target is equal to the cross-sectional area of a metal sphere (i.e., a perfect isotropic scatterer (Norton and Omberg 1947, Kell and Ross 1970)), located at the target's position, which would produce the echo power received from the target. We occasionally consider the total cross section obtained via dual-circular measurements, $\sigma_{TC} \equiv \sigma_{OC} + \sigma_{SC}$. The cross section uncertainty due to random receiver noise is estimated from the noise power within a bandwidth equal to $\hat{B}_{eq}$. This uncertainty is dwarfed, however, by absolute flux calibration errors, which are typically at least 25%.

Normalization of the radar cross sections to the projected area of the target gives the radar albedos, $\hat{\sigma}_{OC}$, $\hat{\sigma}_{SC}$, and $\hat{\sigma}_{TC}$. We also use the circular polarization ratio $\mu_C \equiv \sigma_{SC}/\sigma_{OC}$. Most systematic errors cancel in forming this ratio, so the error in μ_C is dominated by receiver noise in the OC and SC channels. To be conservative, however, we assign the larger of these two cross section errors to *both* cross sections before computing μ_C and its uncertainty. All errors for ratios in this paper have been estimated as described in the Appendix of Ostro *et al.* (1983).

Two asteroids (41 Daphne and 393 Lampetia) were also observed in orthogonal linear polarizations. Here we define cross sections σ_{SL} and σ_{OL}, as well as the total cross section obtained via dual-linear measurements, $\sigma_{TL} \equiv \sigma_{SL} + \sigma_{OL}$. (Note that noise-free dual-linear and dual-circular spectra obtained with identical radar views of the target would yield $\sigma_{TL} = \sigma_{TC}$.)

TABLE III
Radar Properties by Experiment

Target	Obs'n. Year[a]	OC SNR[b]	$\hat{B}_{eq}$ (Hz)[c]	$\hat{B}_{ZC}$ (Hz)[d]	μ_C[e]	σ_{OC} (km^2)[f]	D_{eff} (km)[g]	$\hat{\sigma}_{OC}$[h]	$\lvert\delta_{rad}\rvert$ (°)[i]	λ, β (°)[j]
5 Astraea	1983	23	120 ± 10	180 ± 20	0.20 ± 0.04	2400 ± 600	120 ± 14	0.21 ± 0.08	0–57	159, +3
	1987	24	120 ± 10	175 ± 20	0.20 ± 0.04	2190 ± 550	120 ± 14	0.19 ± 0.07	0–58	131, −1
6 Hebe	1985	8	600 ± 50	—	0.00 ± 0.12	4300 ± 1200	185 ± 10	0.16 ± 0.05	0–54	90, −15
7 Iris	1995 G	60	2350 ± 100	2840 ± 100	0.33 ± 0.04	4700 ± 1200	211 ± 22	0.13 ± 0.04	0–53	69, +3
8 Flora	1981	18	220 ± 20	400 ± 30	0.16 ± 0.05	1500 ± 380	138 ± 9	0.10 ± 0.03	0–23	91, −6
16 Psyche	1980	10	≥520	840 ± 40	0.14 ± 0.10	14000 ± 3700	237 ± 25	0.32 ± 0.12	56–70	78, −5
	1985	16	600 ± 50	875 ± 100	0.18 ± 0.06	14300 ± 3700	241 ± 26	0.31 ± 0.11	52–71	73, −5
18 Melpomene	1985	10	240 ± 20	≥270	0.30 ± 0.09	2000 ± 530	134 ± 22	0.14 ± 0.07	0–58	109, −15
	1995 G	33	680 ± 50	≥810	0.30 ± 0.15	2810 ± 710	141 ± 14	0.18 ± 0.06	0–64	350, −10
19 Fortuna	1982	20	550 ± 30	700 ± 50	0.04 ± 0.04	3200 ± 820	223 ± 41	0.082 ± 0.042	0–59	23, +1
	1986	8	≥330	—	0.12 ± 0.08	2710 ± 710	223 ± 41	0.070 ± 0.036	0–75	58, −1
20 Massalia	1987	11	290 ± 20	≥380	0.28 ± 0.07	2580 ± 670	145 ± 17	0.16 ± 0.06	0–60	69, −1
21 Lutetia	1985	15	41 ± 10	58 ± 10	0.22 ± 0.07	1800 ± 460	116 ± 17	0.17 ± 0.07	76–85	48, −4
27 Euterpe	1986	11	195 ± 10	≥260	0.34 ± 0.08	1110 ± 290	118 ± 21	0.10 ± 0.05	0–64	37, −2
33 Polyhymnia	1985	8	≥55	≥70	0.07 ± 0.11	410 ± 110	62 ± 11	0.14 ± 0.07	0–60	28, +1
41 Daphne	1985	11	≥480	≥540	0.13 ± 0.08	2900 ± 770	187 ± 21	0.11 ± 0.04	0–65	192, +13
46 Hestia	1982	9	≥90	—	0.00 ± 0.11	900 ± 250	124 ± 9	0.074 ± 0.024	0–64	57, −3
78 Diana	1990	9	345 ± 30	465 ± 30	0.00 ± 0.08	1440 ± 380	120 ± 6	0.13 ± 0.04	0–48	122, +10
80 Sappho	1983	18	77 ± 10	170 ± 40	0.25 ± 0.05	650 ± 160	79 ± 10	0.14 ± 0.05	0–62	35, +1
84 Klio	1985	17	80 ± 10	≥105	0.23 ± 0.06	760 ± 190	79 ± 13	0.15 ± 0.07	—	18, +15
97 Klotho	1981	6	45 ± 10	—	—	1100 ± 320	83 ± 10	0.20 ± 0.08	0–71	122, −12
	1993–4 G	14	245 ± 20	310 ± 20	0.23 ± 0.07	1200 ± 310	83 ± 8	0.22 ± 0.08	0–37	111, −18
105 Artemis	1988	28	58 ± 5	≥70	0.15 ± 0.04	1800 ± 440	119 ± 17	0.16 ± 0.07	0–78	247, +38
139 Juewa	1983	8	≥70	—	0.10 ± 0.10	1300 ± 350	164 ± 22	0.061 ± 0.025	0–79[k] or 0–68	141, +10
144 Vibilia	1984	9	≥130	—	0.18 ± 0.10	1800 ± 500	142 ± 13	0.11 ± 0.04	0–70	45, −5
192 Nausikaa	1985	8	90 ± 10	≥115	0.00 ± 0.11	890 ± 240	95 ± 13	0.13 ± 0.05	0–70	358, +5
194 Prokne	1990 G	23	530 ± 15	750 ± 50	0.16 ± 0.04	5200 ± 1300	169 ± 20	0.23 ± 0.09	0–66	312, +18
230 Athamantis	1985	6	≥45	—	0.00 ± 0.12	2080 ± 570	109 ± 14	0.22 ± 0.09	0–76	343, +14
324 Bamberga	1991	30	155 ± 10	≥195	0.14 ± 0.03	2880 ± 860	229 ± 12	0.070 ± 0.021	0–30	346, +11
	1991 G	20	630 ± 40	≥720	0.18 ± 0.05	3030 ± 910	229 ± 12	0.074 ± 0.022		

Table III—*Continued*

Target	Obs'n. Year[a]	OC SNR[b]	$\hat{B}_{eq}$ (Hz)[c]	$\hat{B}_{ZC}$ (Hz)[d]	μ_C[e]	σ_{OC} (km^2)[f]	D_{eff} (km)[g]	$\hat{\sigma}_{OC}$[h]	$\lvert\delta_{rad}\rvert$ (°)[i]	λ, β (°)[j]
356 Liguria	1983	14	72 ± 10	≥115	0.12 ± 0.06	1800 ± 460	131 ± 15	0.13 ± 0.05	0–48	26, +9
393 Lampetia	1986	44	70 ± 5	105 ± 10	0.11 ± 0.02	1550 ± 390	125 ± 10[l] or 97 ± 31	0.13 ± 0.04[l] or $0.21^{+0.40}_{-0.09}$	0–24[l] or 0–64	302, +31
532 Herculina	1987	8	330 ± 40	≥450	0.37 ± 0.15	3000 ± 1500	207 ± 25	0.09 ± 0.05	0–61	185, +28
554 Peraga	1984	14	150 ± 20	≥190	0.06 ± 0.06	1600 ± 400	96 ± 13	0.22 ± 0.09	0–51	15, +5
694 Ekard	1983	8	200 ± 40	≥250	0.00 ± 0.10	610 ± 160	91 ± 13	0.09 ± 0.04	0–73	8, +15
796 Sarita	1991	8	150 ± 20	—	—	390 ± 100	45 ± 6	0.25 ± 0.10	0–60	48, −1

[a] Year of radar observation. Goldstone observations are identified by a G.

[b] The OC SNR is the signal-to-noise ratio for an optimally filtered, weighted sum of all OC echo spectra.

[c] By definition (Tiuri 1964), equivalent bandwidth $B_{eq} = \Delta f[(\sum S_i)^2/\sum S_i^2]$, where S_i are the OC spectral elements and Δf is the "raw" frequency resolution. Wishing to smooth in frequency just enough to minimize the influence of random baseline noise on our estimate, we take unfolded spectra and compute B_{eq} for several frequency resolutions. These values sometimes exhibit large fluctuations at fine resolutions, but they become more stable, and increase slowly and steadily at coarser resolutions. In such cases, stated estimates $\hat{B}_{eq}$ refer to a resolution at the boundary between these two regimes; otherwise we use the raw resolution to obtain $\hat{B}_{eq}$. Uncertainties are subjectively determined by inspecting the fluctuations in B_{eq} near the chosen resolution.

[d] $\hat{B}_{ZC}$ is the zero-crossing bandwidth of the weighted sum of all OC spectra, folded about zero Doppler and smoothed in frequency. The degree of smoothing is determined as described above for $\hat{B}_{eq}$; coarser effective resolution is usually required for obtaining $\hat{B}_{ZC}$ than for obtaining $\hat{B}_{eq}$. Uncertainties are subjectively determined by inspecting the fluctuations in zero-crossing bandwidth B_{ZC} near the chosen resolution.

[e] μ_C is the circular polarization ratio, SC/OC. Standard errors quoted for μ_C are obtained by first determining, for both the SC and the OC spectrum, the standard deviation of the receiver noise in the OC equivalent bandwidth ($\hat{B}_{eq}$). The larger of these two values is used as the standard deviation for both the numerator and the denominator of the polarization ratio, and the error on μ_C is computed accordingly (Ostro *et al.* 1983).

[f] σ_{OC} is the OC radar cross section. Assigned standard errors are the root sum square of systematic calibration errors, estimated as 25% of the cross-section values, and the standard deviation of the receiver noise in the equivalent bandwidth ($\hat{B}_{eq}$).

[g] D_{eff} is the effective diameter of the target. By definition, the mean projected area of the reference ellipsoid as viewed by the radar is equal to $\pi D_{eff}^2/4$. The stated standard error incorporates uncertainties in the axis lengths, differences between IRAS and radar viewing geometries, and rotational phase coverage for the IRAS and radar data.

[h] The radar albedo, $\hat{\sigma}_{OC}$, is equal to $\sigma_{OC}/(\pi D_{eff}^2/4)$. Standard errors propagate from those given for σ_{OC} and D_{eff} (Ostro *et al.* 1983).

[i] Absolute value of the subradar latitude over the duration of radar observations, computed as $\lvert\delta_{rad}\rvert = \cos^{-1}[B/B_{max}(\delta_{rad} = 0)]$. All stated ranges are at the 95% confidence level.

[j] Ecliptic longitude and latitude at the weighted midpoint of radar observations.

[k] Top and bottom entries for 139 Juewa refer to $P = 20.9$ h and $P = 41.8$ h, respectively (see Appendix).

[l] Top and bottom entries for 393 Lampetia refer to $P = 38.7$ h and $P = 19.35$ h, respectively. See text for discussion.

Single scattering from smooth facets produces a purely SL echo, so the linear polarization ratio $\mu_L \equiv \sigma_{OL}/\sigma_{SL}$ depends on multiple scattering and wavelength-scale structure for a nonzero value in much the same way that μ_C does. However, because of the Arecibo telescope's feed rotation between transmit and receive times, the polarization of the "OL" received wave was not orthogonal to that of the transmitted signal, strongly biasing our μ_L estimates upward and undermining their value.

3.3. Radar-Based Pole Constraints

Consider an average of spectra obtained at all rotation phases. As noted earlier, the observed bandwidth B will equal $B_{max}(\delta_{rad} = 0)\cos\delta_{rad}$ in the absence of noise. If we now assume that equality indeed holds, we can use the measured value of B and the inferred value of $B_{max}(\delta_{rad} = 0)$ to determine the subradar latitude:

$$|\delta_{rad}| = \cos^{-1}\left(\frac{B}{B_{max}(\delta_{rad} = 0)}\right). \qquad (10)$$

Given that B and $B_{max}(\delta_{rad} = 0)$ will have associated uncertainties, this relation restricts the object's pole to a pair of annuli on opposite sides of the celestial sphere. When we can place only a lower limit on B, we can still use Eq. (10) to exclude from consideration two circular regions on the sphere, one centered on the target direction and one on the opposite direction.

Unless otherwise stated, our assigned uncertainties are estimated standard errors. In assigning these values, we have tried to account for systematic as well as statistical sources of error in a conservative manner.

4. RESULTS FOR INDIVIDUAL TARGETS

Weighted spectral sums for all radar experiments are displayed in Fig. 1. Echo power, in units of standard deviations of the noise, is plotted vs Doppler frequency. 0 Hz corresponds to echoes from the center of mass, as predicted by our ephemerides.

Table III lists the results (SNR, $\hat{B}_{eq}$, $\hat{B}_{ZC}$, μ_C, σ_{OC}, $\hat{\sigma}_{OC}$, and pole constraints) obtained for each experiment listed in Table II. Table IV gives the average polarization ratio and OC albedo for each MBA radar target, taking into account all data obtained

since 1980. Note that the eight asteroids recently discussed by Mitchell *et al.* (1995, 1996) are included in Table IV. Comments on three targets follow; a number of other targets are briefly discussed in the Appendix.

18 Melpomene

We obtain consistent estimates of radar albedo and polarization ratio for the 1985 Arecibo and 1995 Goldstone experiments. The large polarization ratio indicates considerable near-surface roughness at decimeter scales.

The 3.5-cm data have high enough SNR to reveal a broad spectral feature which shifts from negative to positive Doppler over 60° of rotation. As shown in Fig. 2, this feature is evident on at least two of the three individual dates which covered these rotation phases. Such shifts are predicted for rotating limb-darkened ellipsoids (Jurgens 1982); the middle panels in Fig. 2 would then represent the maximally "end-on" radar view of Melpomene. On this hypothesis we would expect an identical shift one-half rotation later, but these phases were viewed on only one date, so the SNR is insufficient to test the prediction. Hence we cannot rule out the possibility that a nonellipsoidal shape, rather than limb darkening, is responsible for the observed Doppler feature.

Pole constraints derived from the two experiments are depicted in Fig. 3. The two optical pole solutions of Hoffmann and Geyer (1990) have large uncertainties, so neither one is ruled out by the radar data.

21 Lutetia

Mag95 lists the results of six different pole/shape studies and Michałowski (1996) has recently produced a seventh. Two broadly defined prograde rotation states are favored, with each represented by six individual solutions. The individual solutions do not agree well with each other: predictions of subradar latitude range from 42° to 84°. On the other hand, a/b appears to be well determined, with Mag95 giving 1.3 as a "synthesis" value. We adopt this ratio and a standard error of ±0.1, based on the spread of individual estimates. There is poorer agreement for b/c. We discard two extremely high values (1.7 and 2.7) and choose $b/c = 1.15 \pm 0.15$ as an *a priori* estimate.

Our radar observations resulted in the summed spectrum shown in Fig. 1. The bandwidth is $B = \hat{B}_{ZC} = 58 \pm 10$ Hz, where we set the uncertainty to twice the frequency resolution, a subjective but conservative value. With this standard error, the 95% confidence interval from δ_{rad} is $78^\circ \le |\delta_{rad}| \le 85^\circ$.

We now show that corrections for incomplete radar phase coverage cannot significantly weaken this constraint. The instantaneous bandwidth for noise-free spectra and a triaxial ellipsoid target is given as a function of rotation phase ϕ via

$$B(\phi) = B_{max}(\delta_{rad} = 0)\cos\delta_{rad}\sqrt{\cos^2\phi + \left(\frac{b}{a}\right)^2 \sin^2\phi}. \quad (11)$$

Our observations covered about 120° of rotational phase, with only a small (25°) gap within this interval. It is conceivable, but unlikely, that our sampled phases are centered on a minimum-breadth orientation, in which case the square-root factor in the above equation never exceeds 0.948 ± 0.024. The equation would then imply that $\cos\delta_{rad} = B/[(0.948 \pm 0.024)B_{max}(\delta_{rad} = 0)]$. Even if we use the value 0.900 (which is two standard deviations in the direction of weaker pole constraints) in the right-hand-side denominator, we still obtain the restrictive result $76^\circ \le |\delta_{rad}| \le 85^\circ$ at the 95% confidence level.

Figure 4 displays this constraint as a pair of narrow annuli in ecliptic coordinates. The figure also plots the various pole determinations listed in Mag95 and Michałowski (1996). Most of these optically derived solutions are strongly incompatible with the radar data. The exceptions are the solutions published by Michałowski (1993) and by Lagerkvist *et al.* (1995), with the latter results favored. We use these two solutions to revise our reference ellipsoid. The uncertainties in the axis ratios are now larger than had been implied by the full set of optical pole solutions. The two a/b values agree well (1.25 vs 1.22), so we set $a/b = 1.25 \pm 0.15$. The b/c ratios do not agree at all (2.7 vs 1.4), and we feel that Michałowski's result $b/c \approx 2.7 \pm 1.0$ is too inaccurate to be given much weight. We therefore take the Lagerkvist *et al.* value and assign a large subjective error: $b/c = 1.4 \pm 0.3$.

The best pole solution for our revised reference ellipsoid is $(\lambda, \beta) = (228^\circ \pm 11^\circ, +13^\circ \pm 5^\circ)$. The ellipsoid's axis lengths are $130 \times 104 \times 74$ km (with a 17% standard error on the largest diameter $2a$), and the mean projected area viewed by the radar is $\langle A_{proj} \rangle = 10600 \pm 3100$ km^2. The predicted maximum-breadth bandwidth is $B_{max}(\delta_{rad} = 0) = 442 \pm 75$ Hz, yielding the *a posteriori* radar-based pole constraint $76^\circ \le |\delta_{rad}| \le 85^\circ$. A second pole solution at $(\lambda, \beta) = (48^\circ \pm 11^\circ, +5^\circ \pm 5^\circ)$ is in only marginally poorer agreement with the optical and radar data and yields a similar model ellipsoid.

Lutetia has the lowest radar albedo measured for any M-class MBA. This asteroid has already been noted as atypical for its taxonomic class. Its infrared spectrum is unusually flat (Howell *et al.* 1994), and optical polarimetry reveals a large negative polarization depth and inversion angle (Dollfus *et al.* 1989, Belskaya and Lagerkvist 1996). Belskaya and Lagerkvist state that Lutetia's infrared spectrum and polarimetric properties are better explained by a carbonaceous chondritic composition than by metallic composition. Rivkin *et al.* (1997) recently detected the 3-μm water-of-hydration feature, further evidence that Lutetia is largely nonmetallic.

393 Lampetia

Lampetia's rotation period has a factor-of-two ambiguity, with 38.7 h preferred over 19.35 h (Scaltriti *et al.* 1979). Figure 5 shows the phase coverage of our Arecibo data for each of these two possible periods, along with the smoothed, summed spectra obtained on each of the five observing dates. In the central polar

TABLE IV
Average Radar Properties[a]

Target	Class	$\langle\mu_C\rangle$	$\langle\hat{\sigma}_{OC}\rangle$
1 Ceres[b]	G	0.03 ± 0.03	0.041 ± 0.005
2 Pallas[b]	B	0.05 ± 0.02	0.075 ± 0.011
4 Vesta[b]	V	0.28 ± 0.05	0.12 ± 0.04
5 Astraea	S	0.20 ± 0.03	0.20 ± 0.05
6 Hebe	S	0.00 ± 0.12	0.16 ± 0.05
7 Iris[c]	S	0.18 ± 0.10	0.11 ± 0.03
8 Flora	S	0.16 ± 0.05	0.10 ± 0.03
9 Metis[b]	S	0.14 ± 0.04	0.13 ± 0.03
12 Victoria[b]	S	0.14 ± 0.03	0.22 ± 0.05
16 Psyche	M	0.17 ± 0.05	0.31 ± 0.08
18 Melpomene	S	0.30 ± 0.10	0.16 ± 0.05
19 Fortuna	G	0.06 ± 0.04	0.076 ± 0.027
20 Massalia	S	0.28 ± 0.07	0.16 ± 0.06
21 Lutetia	M	0.22 ± 0.07	0.17 ± 0.07
27 Euterpe	S	0.34 ± 0.08	0.10 ± 0.05
33 Polyhymnia	S	0.07 ± 0.11	0.14 ± 0.07
41 Daphne	C	0.13 ± 0.08	0.11 ± 0.04
46 Hestia	P	0.00 ± 0.11	0.074 ± 0.024
78 Diana	C	0.00 ± 0.08	0.13 ± 0.04
80 Sappho	S	0.25 ± 0.05	0.14 ± 0.05
84 Klio	G	0.23 ± 0.06	0.15 ± 0.07
97 Klotho	M	0.23 ± 0.07	0.21 ± 0.06
105 Artemis	C	0.15 ± 0.04	0.16 ± 0.07
139 Juewa	CP	0.10 ± 0.10	0.061 ± 0.025
144 Vibilia	C	0.18 ± 0.10	0.11 ± 0.04
192 Nausikaa	S	0.00 ± 0.11	0.13 ± 0.05
194 Prokne	C	0.16 ± 0.04	0.23 ± 0.09
216 Kleopatra[b]	M	0.00 ± 0.05	0.44 ± 0.15
230 Athamantis	S	0.00 ± 0.12	0.22 ± 0.09
324 Bamberga	CP	0.15 ± 0.04	0.066 ± 0.008[d]
356 Liguria	C	0.12 ± 0.06	0.13 ± 0.05
393 Lampetia	C	0.11 ± 0.02	see text
532 Herculina	S	0.37 ± 0.15	0.09 ± 0.05
554 Peraga	FC	0.06 ± 0.06	0.22 ± 0.09
654 Zelinda[b]	C	0.13 ± 0.03	0.18 ± 0.06
694 Ekard	CP:	0.00 ± 0.10	0.09 ± 0.04
796 Sarita	XD	—	0.25 ± 0.10

[a] Weighted average disk-integrated radar properties from all existing data.
[b] Stated radar properties for 1 Ceres, 2 Pallas, and 4 Vesta are taken from Mitchell *et al.* (1996); those for 9 Metis, 12 Victoria, 216 Kleopatra, and 654 Zelinda are from Mitchell *et al.* (1995).
[c] Stated radar properties for 7 Iris were obtained by combining new data reported here with results derived from earlier experiments by Mitchell *et al.* (1995).
[d] Radar albedo stated for 324 Bamberga incorporates both monostatic and bistatic results from de Pater *et al.* (1994), but has been increased by 10% due to a downward revision of the IRAS diameter estimate (Ted97).

plots in this figure, each radial line segment represents a four-minute block of data which contributed to the spectral sum. The length of the line segment is proportional to the OC or SL rms noise level for those data; the angular position of the line segment is the target's mean rotational phase (relative to an arbitrarily chosen epoch) over that four-minute interval.

We received OC echoes on three dates and SL echoes on two dates, with SNR ranging from 17 to 26 (see Table V). There is no significant day-to-day variation in either σ_{OC} or σ_{SL}, but the weighted mean value of σ_{SL} is about 25% lower than that of σ_{OC}. We also find that σ_{TL} is about 25% lower than σ_{TC}, suggesting a systematic difference in the linear and circular measurements. This difference in cross sections is not due to variations in projected area, as neither of the two phase-coverage patterns depicted in Fig. 5 offers any way to have an elongated Lampetia viewed nearly end-on for both of the SL dates but for none of the three OC dates. If $P = 19.35$ h, we could explain the data by invoking a lower radar albedo for the side of the target viewed on the SL dates (see Fig. 5); yet although we cannot rule out albedo variations, we will see below that this period presents other difficulties. Telescope pointing errors, or else some unidentified system problem, may be responsible for the apparent difference between our σ_{OC} and σ_{SL} estimates.

Bandwidth variations seen over the course of the experiment could help us to resolve the period ambiguity. Hence we created and analyzed weighted spectral sums within various rotation phase intervals. For a 38.7-h period, the top half of Fig. 5 shows that the appropriate phase intervals are those five which correspond to the five observing dates. (We refer to these sums by date and polarization sense: 16 OC, 19 SL, etc.) The 16 OC and 20 SL data overlap in phase if $P = 19.35$ h (Fig. 5, bottom half), so we also analyzed a "16 OC + 20 SL" spectrum that includes all data from both of these dates. (The systematic cross section discrepancy discussed earlier should have little influence on the width of this combined spectrum.)

The maximum lightcurve amplitude of 0.14 mag (Lagerkvist *et al.* 1989) indicates that bandwidth variations are likely to be on the order of 10%. This level of variation reduced the reliability of bandwidth estimates $\hat{B}_{ZC}$, as the zero-crossing bandwidth for a given spectrum varied by 10% depending on how much smoothing in frequency we used and on whether or not we folded the spectrum. Hence we tested a number of other bandwidth estimators, settling on two which were less prone to these problems: the "equivalent bandwidth" estimator (see Section 3.2) and the "two-sigma bandwidth" estimator which measures between the innermost two-sigma crossing points (i.e., the points above and below zero Doppler where the echo power first drops to two standard deviations of the noise). Results are listed in Table V. Although bandwidth differences are present at the 5–10% level, we do not find credible evidence for periodic variations. Hence the bandwidth estimates do not favor either rotation period.

Figure 5 clearly shows that there is real variation in spectral shape. Subtracting one side of each spectrum from the other side (not shown) confirms that statistically significant off-center peaks exist for some spectra. We chose not to use the skew statistic to quantify this asymmetry, because that estimator is highly sensitive to noise fluctuations near the spectral edges. Instead we computed the three location parameters given in Table V: the midpoint frequency $f_{2\sigma}$ between the innermost two-sigma crossing points; the median f_{med} (which has half the integrated echo to each side); and the peak f_{peak} of the maximum signal. A spectrum with positive skew—that is, one which has an

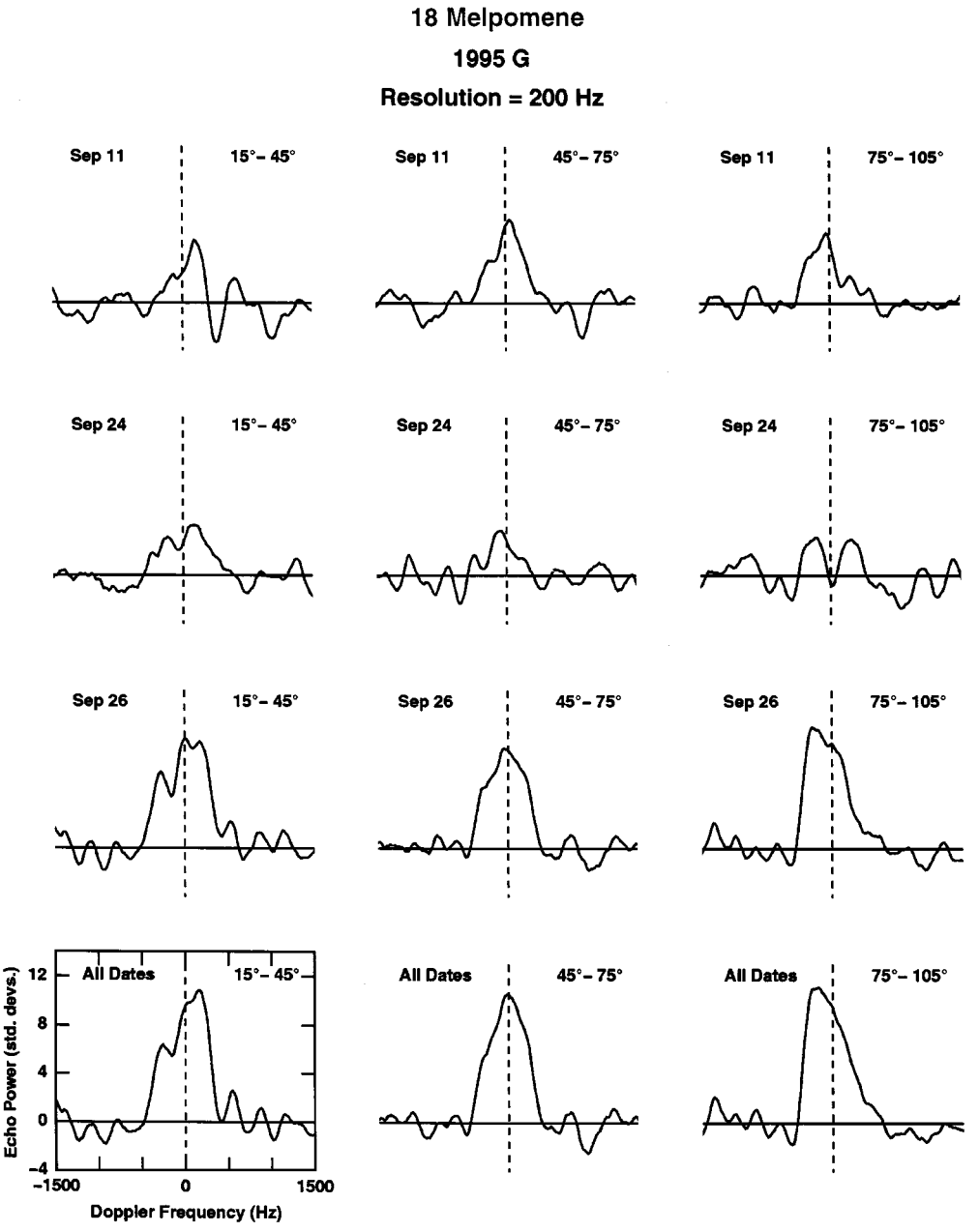

FIG. 2. Weighted sums of 1995 OC echo spectra of 18 Melpomene within three adjacent rotation phase intervals. The four rows display these sums for three different observing dates and for the combined dates. All 12 plots are on the scale indicated at lower left.

extended positive-frequency tail—would have $f_{2\sigma} > f_{\text{med}} > f_{\text{peak}}$. This relation is in fact observed for 19 SL and 20 SL, while we see the opposite trend (negative skew) for 16 OC and 17 OC. Of the five single-date spectral sums, only 18 OC is nearly symmetric.

This skew is important because it is in opposite senses for 16 OC and 20 SL, as seen both in Fig. 5 and in Fig. 6, thus explaining why the "16 OC + 20 SL" spectrum is symmetric by the criterion described above. The bottom half of Fig. 5 indicates that the views on these two dates were almost identical for a 19.35-h period, so it is difficult to see why they should produce different spectral shapes. Unfortunately, the changes in asymmetry do not easily fit a 38.7-h period, either. For example, if Lampetia were a limb-darkened ellipsoid, the echo's shape and centroid would vary at twice the rotation frequency (Jurgens 1982), leading us to predict (incorrectly) the same shape for 16 OC and 20 SL (see Fig. 5, top half). Those two spectra could be explained by a lopsided target—say, an ovoid—but we then would expect the 17 OC and 19 SL echoes to look more like the 20 SL and 16 OC echoes, respectively, contrary to what is actually observed.

In all, our data indicate that Lampetia is not spherical, not uniformly scattering, or both, but the SNR and (more importantly)

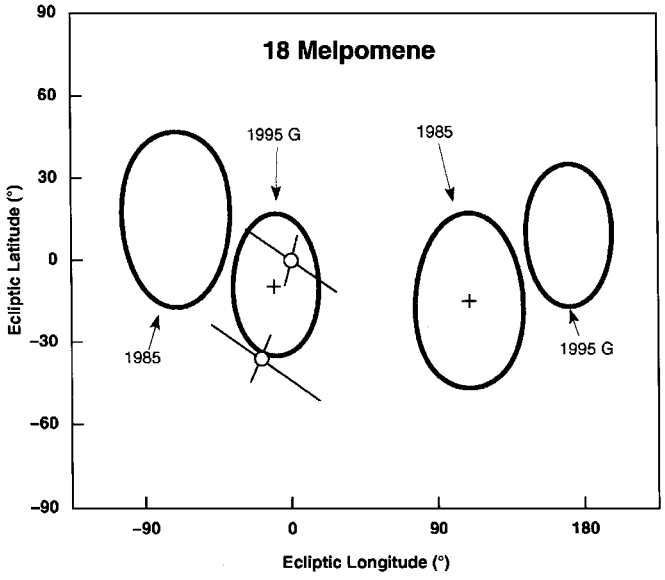

FIG. 3. Comparison of radar and lightcurve constraints on 18 Melpomene's pole direction shown in a rectangular projection of ecliptic coordinates. The target's position on the sky during each radar experiment is shown by a plus symbol, and the pole constraints for each experiment taken separately are shown by a pair of circles, one centered on the target's position and one on the antipodal position. These circles are defined (Eq. 10) by the ratio of measured bandwidth B to predicted maximum-breadth bandwidth $B_{\max}(\delta_{\rm rad} = 0)$. Predicted bandwidths are 404 ± 52 Hz (1985) and 1450 ± 190 Hz (1995 G). Lower bounds on B are 270 Hz (1985) and 810 Hz (1995 G); these limits constrain the pole to lie outside each of the four circles (at the 95% confidence level). The two optical pole solutions of Hoffmann and Geyer (1990), and the quoted uncertainties, are plotted as open circles with error bars.

rotational phase coverage are insufficient to support more specific conclusions about shape. Hence we are unable to resolve the period ambiguity, and we will examine the implications of each candidate period for interpretations of the radar cross section and bandwidth of our multidate OC spectral sum.

a. $P = 38.7$ h. We estimate that $B = \hat{B}_{\rm ZC} = 105 \pm 10$ Hz. Inserting this bandwidth and a 38.7-h period into Eq. (8), we find that the target's maximum breadth is given by $D_{\max} \geq (146 \pm 14\,{\rm km})/\cos\delta_{\rm rad}$. We now set $D_{\max}$ equal to $(146 \pm 14$ km$)/\cos\delta_{\rm rad}$, keeping in mind that off-center rotation would make this an overestimate while incomplete phase coverage could make it an underestimate.

Given the IRAS diameter estimate of 97 ± 31 km, we can best satisfy this relation for $D_{\max}$ by maximizing $\cos\delta_{\rm rad}$—that is, by setting $\delta_{\rm rad} \approx 0$ (equatorial view). On this assumption, the radar data indicate that Lampetia's maximum breadth is 146 ± 14 km, and hence we must rule out the lower half of the IRAS confidence interval (97 ± 31 km) as extremely unlikely. Data for two of the three IRAS sightings in fact indicate a diameter of roughly 125 km, while the third gives 45–75 km. The radiometric TRIAD diameter estimate (Bowell *et al.* 1979) is 117 km. Combining our radar estimates with the infrared data (but ignoring the third IRAS sighting) leads to an equivalent spherical diameter $D_{\rm eff} = 125 \pm 10$ km, which we use in our analysis.

b. $P = 19.35$ h. Radar constraints on Lampetia's physical properties are much less interesting if the shorter period is correct. For example, repeating the preceding analysis for this period leads to the result $D_{\max} = (73 \pm 7\,{\rm km})/\cos\delta_{\rm rad}$. If we now equate this to the IRAS diameter estimate $D_{\rm IR} = 97 \pm 31$ km, we obtain the 95% confidence interval $|\delta_{\rm rad}| \leq 64^\circ$ for the

TABLE V
Radar Data for 393 Lampetia by Rotation Phase Interval[a]

Interval	SNR	$\sigma_{\rm pol}$ (km^2)	$\sigma_{\rm tot}$ (km^2)	μ	$\hat{B}_{\rm eq}$ (Hz)	$\hat{B}_{2\sigma}$ (Hz)	$f_{2\sigma}$ (Hz)	$f_{\rm med}$ (Hz)	$f_{\rm peak}$ (Hz)
16 OC	26	1690 ± 61	1780 ± 63	0.05 ± 0.04	70	79	−4.0	1.5	5.7
17 OC	24	1490 ± 56	1730 ± 67	0.16 ± 0.04	65	74	−3.4	6.5	17.0
18 OC	25	1490 ± 56	1670 ± 62	0.13 ± 0.04	66	80	2.3	2.5	−2.9
19 SL	20	1190 ± 56	1390 ± 64	0.16 ± 0.05	60	71	−0.5	−3.8	−11.4
20 SL	17	1070 ± 58	1140 ± 59	0.07 ± 0.06	69	77	3.4	0.8	−2.9
16 OC + 20 SL[b]	30	—	—	—	72	87	−0.8	1.3	0.0
16–18 OC	44	1550 ± 35	1730 ± 42	0.113 ± 0.023	70	91	3.7	3.2	0.0
19–20 SL	26	1130 ± 42	1260 ± 46	0.117 ± 0.037	65	79	1.5	−1.5	−2.9

[a] Listed parameters include the SNR of the "polarized" (OC and/or SL) spectral sum; the polarized cross section $\sigma_{\rm pol}$; the total (polarized + depolarized) cross section $\sigma_{\rm tot}$; the polarization ratio μ = depolarized/polarized; the "equivalent bandwidth" estimate $\hat{B}_{\rm eq}$; the "two-sigma bandwidth" estimate $\hat{B}_{2\sigma}$ measured between the innermost two-sigma crossing points (i.e., the points above and below zero Doppler where the echo power first drops to two standard deviations of the noise); the frequency $f_{2\sigma}$ midway between the innermost two-sigma crossing points; the median frequency $f_{\rm med}$, for which half of the integrated signal is at higher frequencies and half at lower; and the frequency $f_{\rm peak}$ at which the peak signal occurs. All parameters were computed for unfolded spectra. Cross sections, polarization ratios, and $f_{\rm med}$ were computed for unsmoothed ($\Delta f = 2.8$ Hz) spectra; $\hat{B}_{2\sigma}$ and $f_{2\sigma}$ were computed for spectra smoothed to 10 Hz resolution; $f_{\rm peak}$ was computed for 20 Hz resolution. Listed $\hat{B}_{\rm eq}$ values correspond to 2.8 Hz resolution for multidate sums, and roughly 5 Hz for individual dates. These resolution values were chosen through the same procedure described for $\hat{B}_{\rm eq}$ in footnote c of Table III. Listed cross section standard errors reflect only the contributions of receiver noise, as appropriate for date-to-date comparisons.

[b] Due to systematic discrepancies between OC and SL cross sections (see text), no cross section or polarization ratio estimates are given for the combined "16 OC + 20 SL" spectrum.

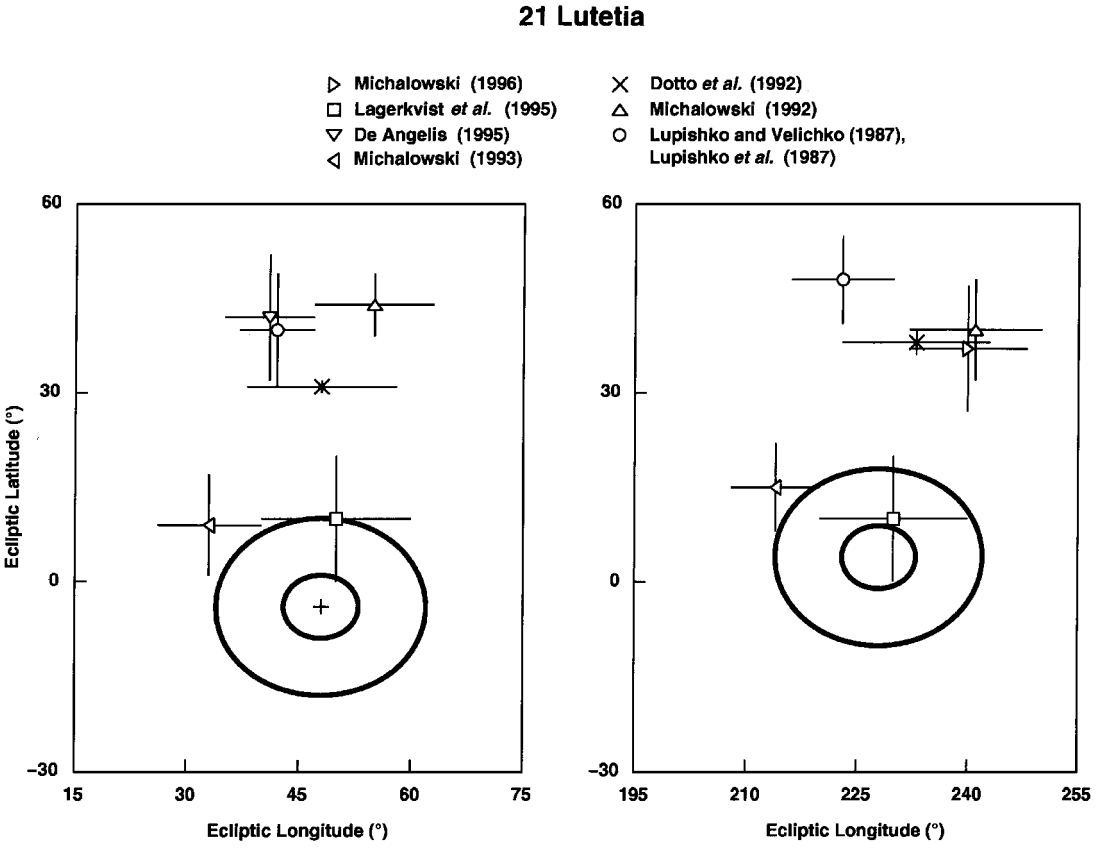

FIG. 4. 21 Lutetia pole constraints; see Fig. 3 caption. Radar data constrain the pole to lie within the two annuli (at the 95% confidence level). These annuli are defined (Eq. 10) by the ratio of measured bandwidth $B = 58 \pm 10$ Hz to predicted maximum-breadth bandwidth $B_{\max}(\delta_{\rm rad} = 0) = 442 \pm 75$ Hz. See text for further discussion. Optical pole solutions and quoted uncertainties are plotted as open symbols with error bars; see legend.

subradar latitude. Hence unless we make additional assumptions, we can place no new constraints on the diameter and only weak constraints on the pole direction.

5. STATISTICAL ANALYSES

Table VI lists means, standard deviations, ranges, and sample sizes for $\mu_{\rm C}$ and $\hat{\sigma}_{\rm OC}$ as a function of taxonomic class. In addition to the 5 M objects, the 14 S objects, the 7 C objects, and 4 Vesta (V), we have 9 objects which are listed as B, FC, G, P, or CP by Tholen (1989). The B, F, G, and P classes are similar to the C class in that they are considered mineralogically associated with primitive meteorites (Bell *et al.* 1989, Gaffey *et al.* 1989); here we group them into the "BFGP" class for analysis purposes. BFGP, in other words, consists of primitive radar targets which are not, or might not be, type C. Note that this group includes 7 of the 9 "C" objects discussed by Ostro *et al.* (1985).

5.1. Correlations between Radar/Optical Properties

Figure 7 displays our estimated radar albedos and polarization ratios plotted as functions of radiometric diameter $D_{\rm IR}$ and visual geometric albedo p_V. For each of the variable pairs represented in these plots, linear regression analysis (Table VII) yields the probability that the null hypothesis (uncorrelated variables) is valid. Small listed probabilities imply that we should instead favor the alternative hypothesis (correlated variables).

The last column of Table VII indicates that for the full sample of 37 objects, the trends that are significant (at the 95% level or

TABLE VI
Radar Parameters by Taxonomic Class[a]

	$\mu_{\rm C}$				$\hat{\sigma}_{\rm OC}$			
Class	Mean	*SD*	range	*N*	Mean	*SD*	range	*N*
BFGP	0.076	0.075	0.23	9	0.095	0.056	0.18	9
C[b]	0.123	0.054	0.18	8	0.150	0.044	0.12	7
S	0.174	0.125	0.37	14	0.147	0.043	0.13	14
M	0.155	0.107	0.23	4	0.276	0.105	0.27	5
V	0.28	—	—	1	0.12	—	—	1
All	0.139	0.104	0.37	36	0.152	0.078	0.40	36

[a] Means, standard deviations, ranges, and sample sizes for polarization ratio and radar albedo, listed as a function of taxonomic class. Nine asteroids classified as B, FC, G, P, and CP by Tholen (1989) are grouped here as the "BFGP" sample. 796 Sarita has been included in the M class.

[b] Due to period ambiguity, 393 Lampetia's radar albedo is highly uncertain (see Table III) and is not included in our analysis.

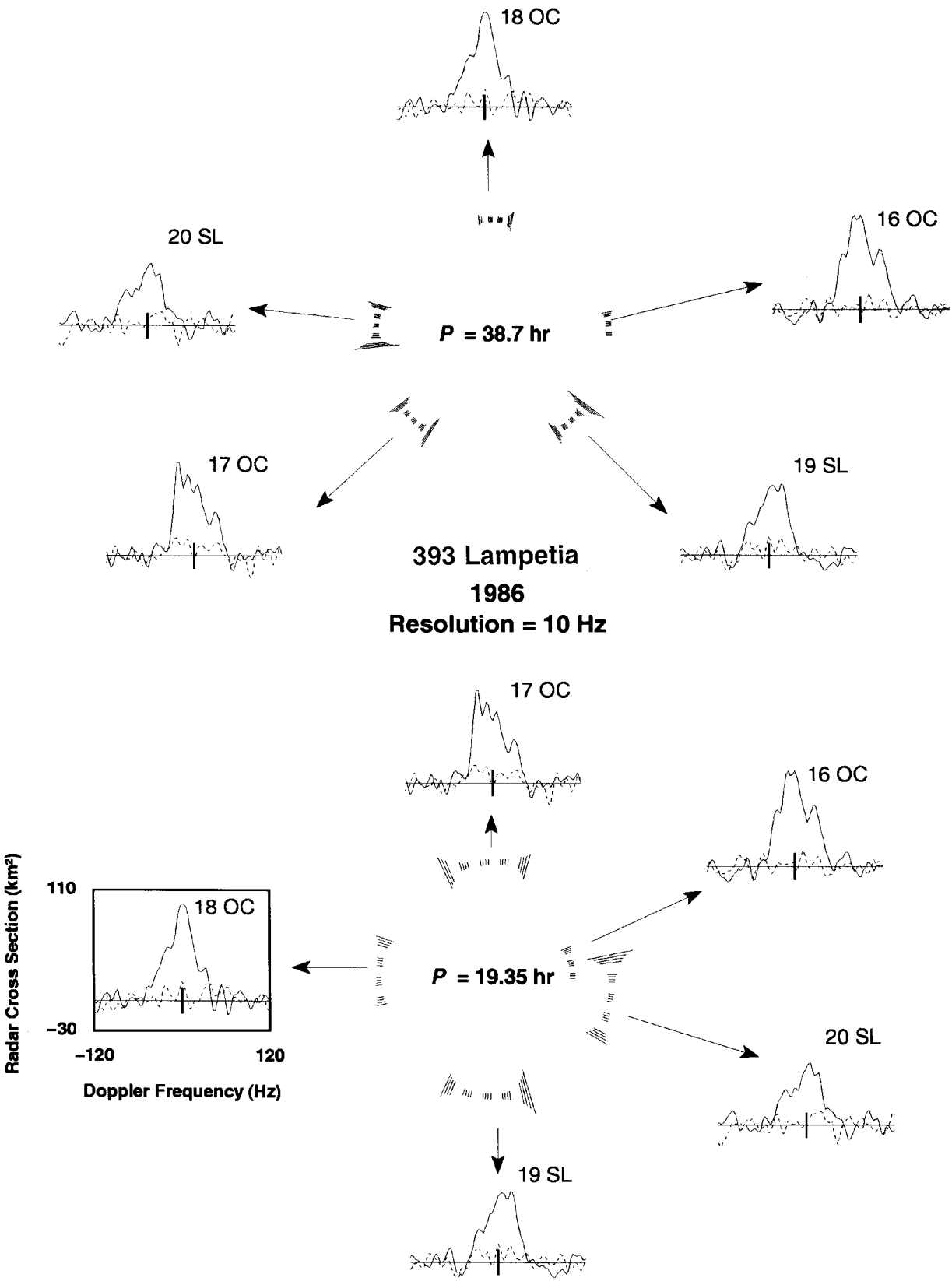

FIG. 5. Weighted sums of echo spectra of 393 Lampetia for each of the five observing dates. All plots are on the scale indicated at lower left. The vertical axis represents radar cross section per raw frequency element ($\Delta f = 2.8$ Hz). The vertical bar at the origin indicates ± 1 standard deviation of the OC or SL noise. The central plot in the top half of the figure depicts rotation phase coverage for an assumed period of 38.7 h; see Fig. 1 caption. Arrows connect each of the five single-date sums with the corresponding rotation phase interval. The bottom half of the figure is the same as the top, except that a 19.35-h period is assumed.

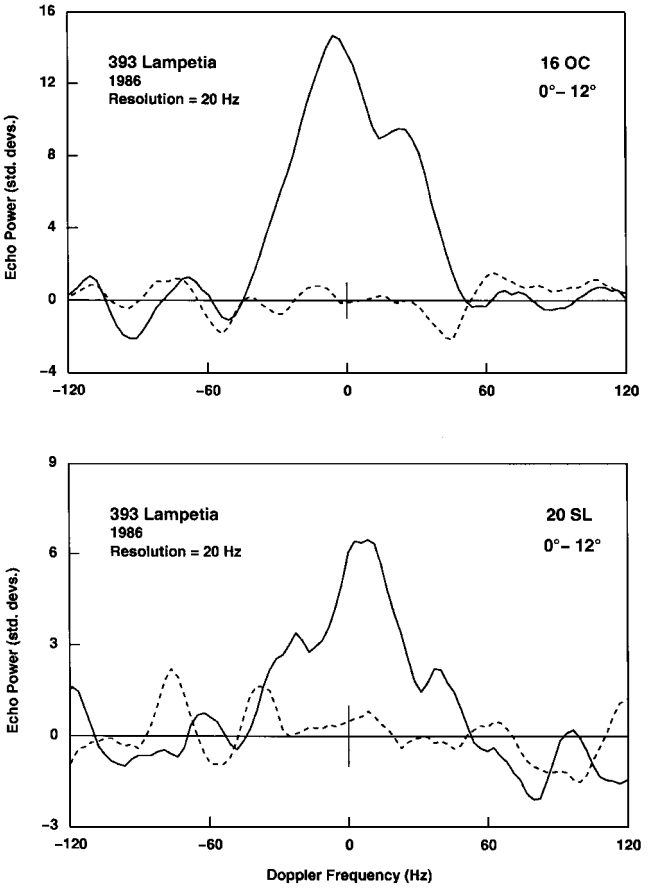

FIG. 6. Weighted sums of dual-circular and dual-linear polarization echo spectra of 393 Lampetia for 1986 July 16 and 20, respectively, for the rotation phase range 0°–12° (assuming a 19.35-h period). Solid lines denote OC and SL spectra, while dashed lines show SC and OL data. The vertical bar at the origin indicates ±1 standard deviation of the OC or SL noise.

higher) are that μ_C is correlated with p_V while $\hat{\sigma}_{OC}$ is anticorrelated with D_{IR}. Yet if we remove 1 Ceres from the latter analysis, the significance of the trend is lowered from 95.5 to 92.5%. Similarly, ignoring the high-μ_C object 4 Vesta reduces the significance of the μ_C vs p_V correlation from 97.5 to 83%. Hence these trends are, at most, marginally significant. Within individual classes, the only significant relationship we find is that $\hat{\sigma}_{OC}$ is anticorrelated with p_V for the five M-class objects. (Note, however, that in checking four variable pairs for each of four classes, we expect about one significant correlation at the 95% level even if no correlations actually exist in the parent asteroid populations. See Section 5.3 for further discussion.) We conclude that interclass comparisons of radar scattering properties will be little influenced by underlying dependencies on D_{IR} and p_V .

TABLE VII
Probabilities Derived from Linear Regression Analysis[a]

	BFGP	C	S	M	All
μ_C vs D_{IR}	0.50	0.37	0.34	0.81	0.64
μ_C vs p_V	0.66	0.36	0.49	0.22	0.025
$\hat{\sigma}_{OC}$ vs D_{IR}	0.16	0.78	0.20	0.49	0.045
$\hat{\sigma}_{OC}$ vs p_V	0.36	0.16	0.45	0.044	0.77
$\hat{\sigma}_{OC}$ vs μ_C	0.49	0.63	0.16	0.046	0.71

[a] Probabilities that the null hypothesis of uncorrelated variables is valid. Small values indicate significant correlations between variables.

Figure 8 shows polarization ratio as a function of OC albedo for all radar targets. Linear regression (Table VII) shows that there is no significant correlation for the full sample. The only single-class trend which is significant at the 95% level is for the M-class MBAs, due primarily to the high-albedo, low-μ_C object 216 Kleopatra.

5.2. Interclass Comparisons: Histograms

Do the different taxonomic classes have different distributions of radar albedo or polarization ratio? The four classes considered are those for which we have more than one member: BFGP, C, S, and M. Figure 9 shows the univariate μ_C and $\hat{\sigma}_{OC}$ distributions for each of these classes. The corresponding distributions for the full sample (including 4 Vesta) are displayed in Fig. 10. Noteworthy features include the broad, flat μ_C distribution for S-class MBAs, the low albedos and polarization ratios for BFGP, the high mean M-class albedo, and the similarity between $\hat{\sigma}_{OC}$ distributions for C and S objects.

Restricting our attention to the albedo histograms, we see that there is only slight overlap between BFGP and M, and that the mean albedo is significantly higher for the M-class objects. These two populations clearly differ in their $\hat{\sigma}_{OC}$ properties. Another firm conclusion is that there is very little difference between the S and C distributions. (Note that the means and standard deviations listed in Table VI are nearly identical.) Other comparisons are more ambiguous—for example, whether M-class MBAs have higher albedos than S-class objects, or whether the albedos of primitive C and BFGP classes differ significantly from each other.

5.3. Interclass Comparisons: Statistical Tests

These visual impressions cannot substitute for interclass statistical tests. Furthermore, we cannot just carry out six pairwise comparisons between our four samples. Suppose, for example, that the four $\hat{\sigma}_{OC}$ samples were drawn from *identical* parent populations. Let us now compare two sample means at a time—using, say, a *t* test (Zar 1996, pp. 123–130)—and let us adopt the 95% significance level. We will then have a 0.95 probability of accepting the null hypothesis (equal population means) if the two population means are in fact equal. Given that we have postulated identical parent distributions, this amounts to a 0.95 probability of obtaining the right answer. If each of three independent comparisons (for example, M vs BFGP, M vs C, and M vs S) has a 0.95 probability of yielding the correct answer, the probability that *all three* (independent) results are correct is only $(0.95)^3 \approx 0.86$. There is, in other words, a 14% chance of incorrectly finding at least one difference between these three

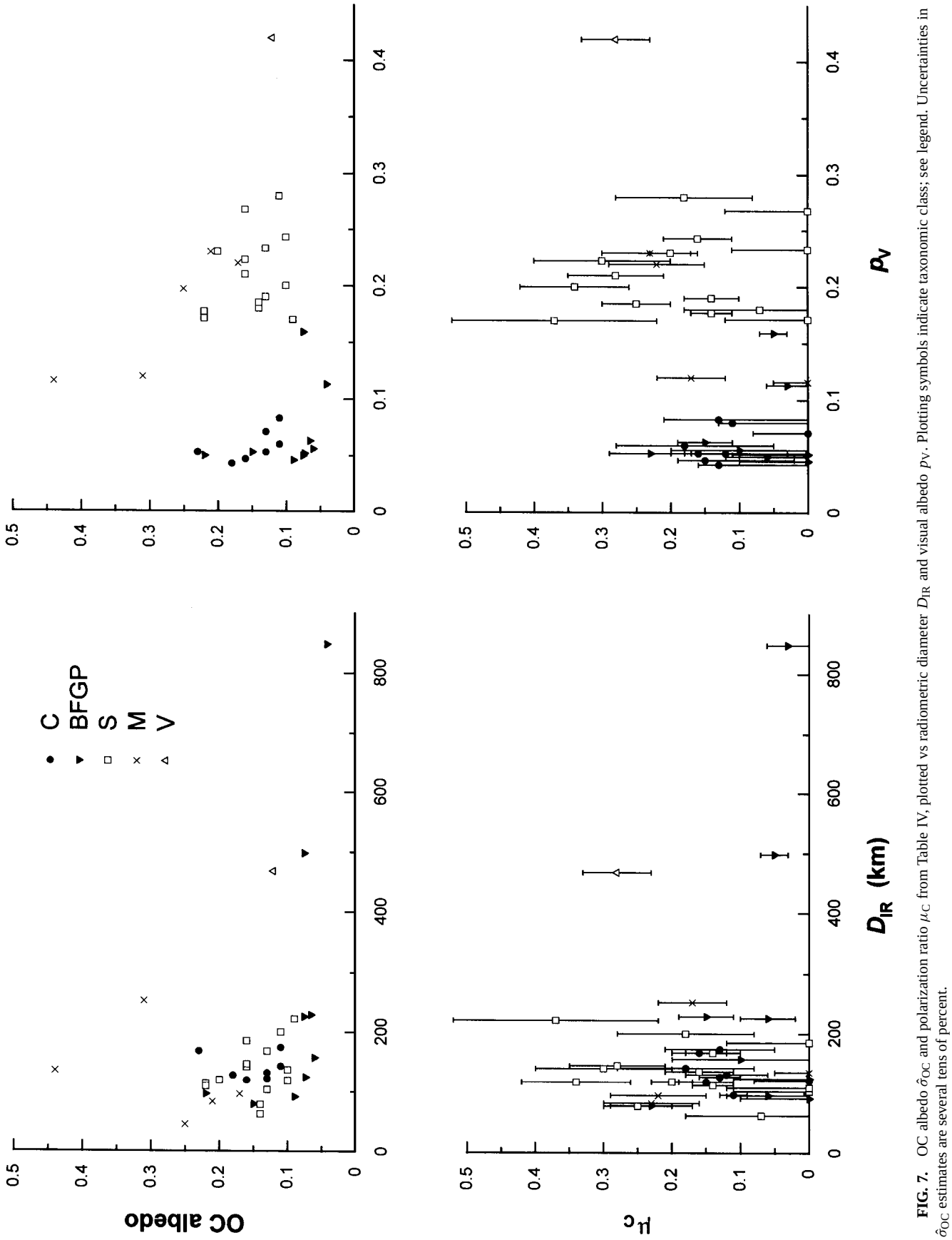

FIG. 7. OC albedo $\hat{\sigma}_{OC}$ and polarization ratio μ_C from Table IV, plotted vs radiometric diameter D_{IR} and visual albedo p_V. Plotting symbols indicate taxonomic class; see legend. Uncertainties in $\hat{\sigma}_{OC}$ estimates are several tens of percent.

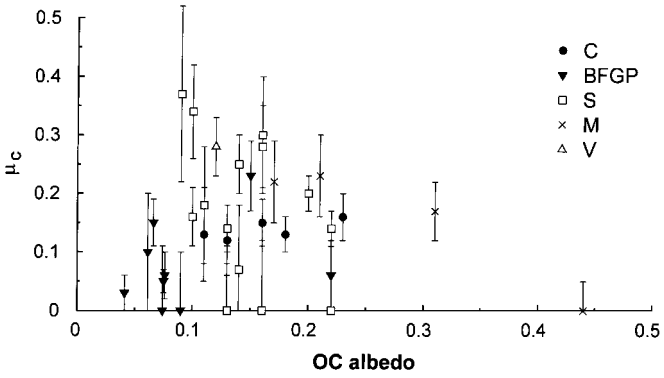

FIG. 8. Polarization ratio μ_C plotted vs OC albedo $\hat{\sigma}_{OC}$ (Table IV). Plotting symbols indicate taxonomic class; see legend.

pairs of means. The rest of the calculation is complicated by the fact that the other three pairwise tests are not independent of the first three. For example, accepting the null hypothesis for M vs S and for M vs C implies that the S and C means are not extremely different from each other, so the probability of concluding that they are identical is about 0.97 rather than only 0.95. For the relatively simple case of equal-size samples with normally distributed means, the probability of correctly accepting the null hypothesis for all six comparisons is 0.80.

Hence a test with a 5% chance of yielding "false positives" (Type I errors) can yield an overall error rate of 20% when applied to six sample pairs. Essentially, the more samples we draw, the greater the probability that we will obtain at least one unrepresentative sample skewed toward extreme values. Note that we cannot remedy this problem by increasing sample sizes. Larger samples are indeed less likely to have a large fraction of members with inordinately high (or low) values; but tests carried out on pairs of such samples are sensitive to smaller differences since the standard errors on the sample means are smaller. We conclude that we must consider all four classes simultaneously, rather than inspecting Table VI for potentially interesting differences and then applying two-sample tests.

Let us first analyze the radar albedo data. All statistical test results (probabilities) discussed below are listed in Table VIII. In that table, moderate and large probabilities indicate samples whose distributions are similar to each other or to a specified theoretical distribution, whereas small probabilities imply significant differences.

Because our samples are small, skewed, or both, it is dangerous to assume that they are drawn from a normal distribution. Hence we rely on robust and nonparametric tests, as implemented in the Prophet 5.0 statistical software package (see http://www.prophet.abtech.com/). The Shapiro–Wilk test (Conover 1980, pp. 363–366) is used to evaluate whether or not a given population is normally distributed; this test measures how well the ordered data for that sample agree with the "normal scores," that is, with the expected ordered values for a sample of equal size taken from a normal distribution. (We do not use the Kolmogorov goodness-of-fit test because it is overly conservative when the mean and variance of the hypothesized normal distribution must be estimated from the data (Conover 1980, p. 357).) For the BFGP sample, the probability that the null hypothesis (normal parent distribution) is valid is only 0.013, so we conclude that it is unsafe to accept this hypothesis. Looking at Fig. 9, we see that two of the nine BFGP members, 84 Klio and (especially) 554 Peraga, have albedos much higher than those of the other seven, giving this distribution a marked positive skew.

To check whether or not the population variances can be considered equal, we use Levene's test (Snedecor and Cochran 1980, pp. 253–254). This test is less sensitive to outliers than the analysis of variance (ANOVA) F test, because it relies on absolute values of deviations from the class mean rather than on squared deviations. We obtain a 0.077 probability that the null hypothesis of equal variances is valid; this value is sufficiently large that we need not reject the hypothesis. Thus we can consider the possibility that the four distributions are identical except for location shifts. For this purpose, we use a Kruskal–Wallis test, a nonparametric analog to one-way ANOVA which operates on ranks rather than on the estimated radar albedos themselves (Daniel 1990, pp. 226–231, Zar 1996, pp. 197–202). The null hypothesis that the four population medians are identical has only a 0.0013 probability of being valid, so we can be confident that at least one of the six possible sample pairs shows a significant difference. The Kruskal–Wallis test itself does not reveal which one(s) of the six is (are) different, so we apply a *post hoc* (multiple comparisons) test. The Dunn *post hoc* test (Zar 1996, p. 227) shows that the BFGP and M classes are likely to have different median radar albedos (Table VIII).

Since different statistical tests can yield different results, it would be useful to subject the data to ANOVA in addition to the Kruskal–Wallis test; we could have greater confidence in any differences or similarities implied by more than one test. In order to apply ANOVA, we first must find a data transformation which reduces the skew of the BFGP distribution without increasing the differences between the four sample variances. We find via trial and error that the transformation $s = \ln(\hat{\sigma}_{OC} + 0.05)$ meets these requirements. The Shapiro–Wilk test now tells us that it is fairly safe to assume normality for all four classes, and Levene's test yields a high probability that the four population variances are equal. Hence we can use one-way unblocked ANOVA (Zar 1996, pp. 180–191) on the transformed data. (This test is slightly more powerful than Kruskal–Wallis if the distributions are indeed normal.) The null hypothesis that the four distributions are identical is highly improbable, leading us to favor the alternative hypothesis that at least two of the four distributions have different means.

Inferences about which samples differ from which others depend on which *post hoc* test we use. Both the liberal Newman–Keuls test and the moderately conservative Tukey "honestly significant difference" test (Zar 1996, pp. 212–218) imply, at the 95% significance level, that the BFGP class differs from the S

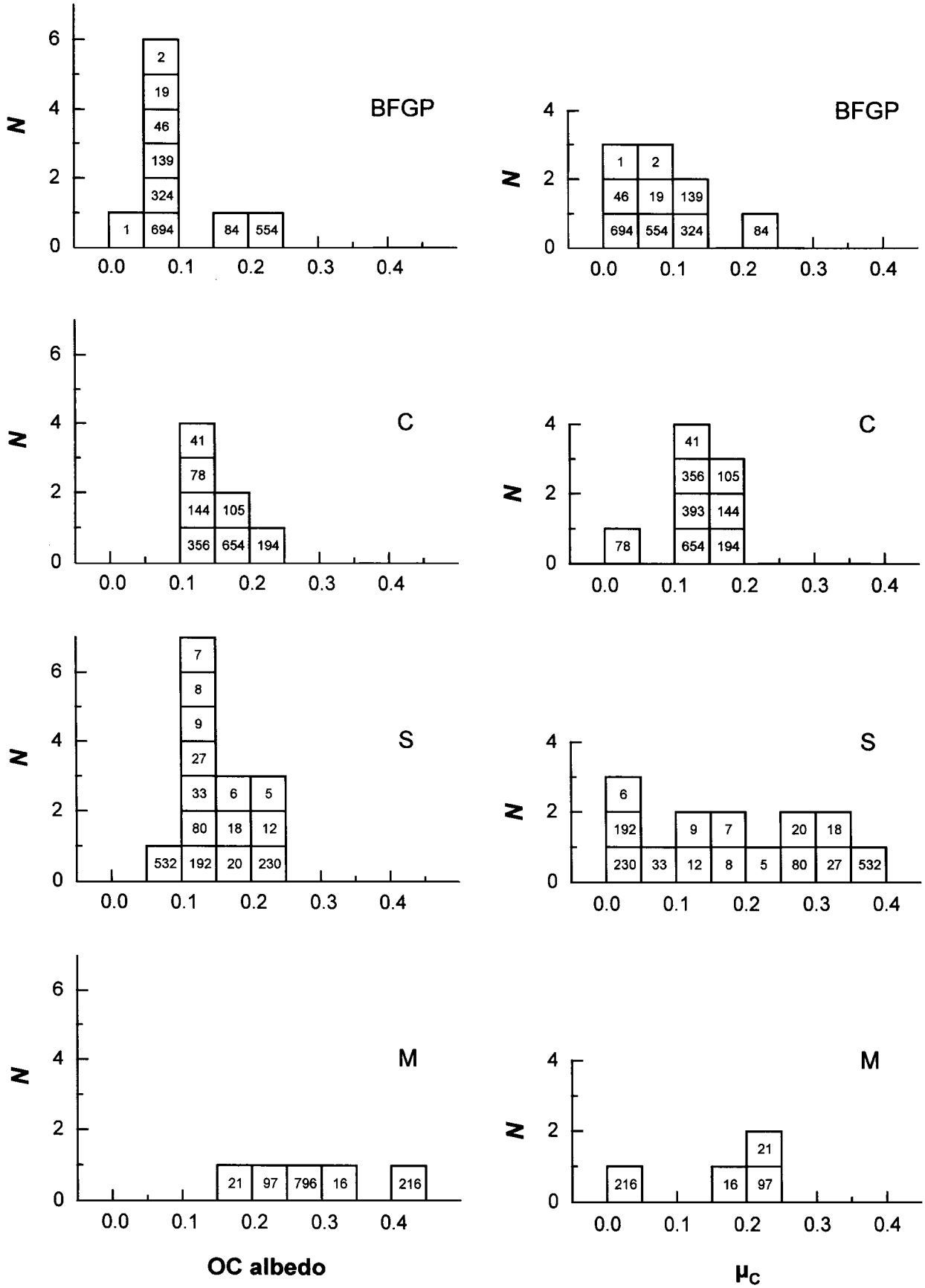

FIG. 9. Histograms of the OC albedo $\hat{\sigma}_{\rm OC}$ and polarization ratio $\mu_{\rm C}$ distributions for the BFGP, C, S, and M-class samples. Each bin is 0.05 wide and includes the lower but not the upper endpoint. Each cell is labeled by the corresponding asteroid number.

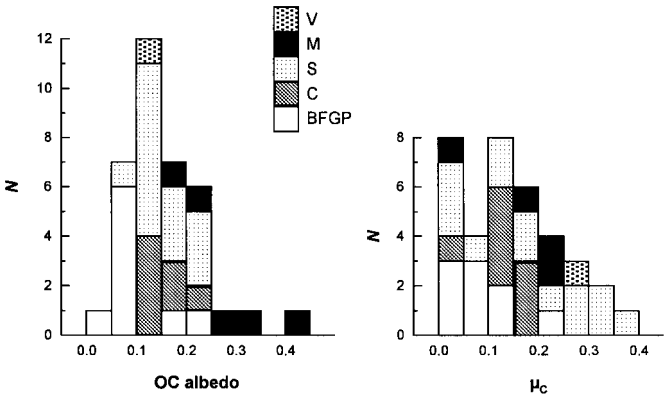

FIG. 10. Histograms of the OC albedo $\hat{\sigma}_{OC}$ and polarization ratio μ_C distributions for all MBA radar targets. Each bin is 0.05 wide and includes the lower but not the upper endpoint. Contributions of the various taxonomic classes are indicated.

and C classes, and that all three differ from the M class. Yet the highly conservative Scheffé test (Zar 1996, pp. 222–225) indicates only that the S and BFGP classes differ from each other and that the M class differs from the other three. Evidently, reliable determination of whether or not C-class MBAs have higher radar albedos than other primitive asteroids hinges on our obtaining larger samples.

Table VIII also lists similar results for various combinations of OC and SC albedo. We carry out a Kruskal–Wallis test whenever Levene's test indicates greater than 5% probability of equal variances. To use ANOVA, we also require a data transformation that yields four approximately normal distributions with similar variances. Blank table entries represent violations of one or more of these conditions.

Results for total albedo $\hat{\sigma}_{TC}$ are similar to those just described for $\hat{\sigma}_{OC}$, as expected for a sample of low-μ_C MBAs. We also compute the difference $\hat{\sigma}_{OC} - \hat{\sigma}_{SC}$, which is proportional to the echo power due to single-scattering from surface elements smooth on the wavelength scale, under the assumption that all other scattering processes contribute a randomly polarized signal. While the M-class objects still differ from BFGP and from S, no other reliable differences are present for this variable. Single scattering from wavelength-scale structure can produce a variety of SC/OC ratios, and therefore we have also considered the variables $\hat{\sigma}_{OC} - 2\hat{\sigma}_{SC}$ and $\hat{\sigma}_{OC} - 3\hat{\sigma}_{SC}$. Most of the corresponding entries in Table VIII are blank, however, because the variance of the M sample is much larger than that of the other three. The object most responsible for this problem is 216 Kleopatra, which has the largest OC albedo (0.44) of any MBA, but which has $\hat{\sigma}_{SC} = 0$. Hence we cannot use Kruskal–Wallis or ANOVA to look for interclass differences here, although, of course, this large variance is itself a significant difference between M-class and other asteroids.

Taking the Kruskal–Wallis and ANOVA results together, we conclude that there is good reason to believe that M asteroids tend to have higher radar albedos and a wider range of albedos than do the other three classes; there is no evidence that C and S MBAs have different albedo distributions; and there is some suggestion, worthy of future study, that BFGP asteroids are radar-darker than are C and S objects.

We can apply a similar analysis to the polarization ratios (Table VIII). The presence of a zero value for 78 Diana gives the C distribution a strong negative skew, and the Shapiro–Wilk test indeed indicates that this distribution is nonnormal. Levene's test allows us to assume equal variances, despite the fact that the seven C-class objects other than Diana have a narrow range of μ_C values. (Evidently the C-class sample is too small for us to assume that Diana is merely a fluke outlier to a narrow distribution.) With equal variances assumed, we can apply a Kruskal–Wallis test; the result is that no credible differences between medians are present. In particular, the Kruskal–Wallis test fails to confirm the visual impression that BFGP objects have especially low μ_C values (Section 5.2). We cannot transform the data so as to reduce the skew—say, by squaring the μ_C values—because such a transformation would increase the disparities between the sample variances. As a result we cannot apply one-way ANOVA to these data. We conclude that there currently is no convincing evidence that different taxonomic classes have different polarization-ratio distributions.

An anonymous reviewer has noted the large number of high-μ_C S-class objects (Fig. 10), which might be taken as evidence that S-class MBAs have higher polarization ratios than do the other three classes. We feel that it is risky to choose a one-tailed hypothesis after the data have been collected and inspected. For example, although our C-class sample has no high-μ_C members, the parent distribution might have *two* broad tails, with only 78 Diana ($\mu_C = 0$; see Fig. 9) sampled from those tails. (This is what Levene's test is telling us when it fails to confirm any difference between variances.) Similar comments apply to the M-class sample and 216 Kleopatra. The BFGP sample has one high-μ_C member, 84 Klio; we do not know how broad the tail represented by this object is. Until larger samples are available, we will restrict our tests to low-order statistics such as means, medians, and variances.

Throughout these analyses we have not made use of the estimated errors on μ_C and $\hat{\sigma}_{OC}$ listed in Table IV. In principle we could perform numerous simulations using "bootstrap" resampling (e.g., Efron and Tibshirani 1993). Each simulation would start with the creation of a 37-member numerical sample; the radar albedos and polarization ratios would be randomly drawn (with replacement) from normal distributions whose means and standard deviations are set equal to the estimates and one-sigma errors listed in Table IV. We then would subject each such sample to the same analysis described above and would thereby estimate the probability that the interclass differences in $\hat{\sigma}_{OC}$ could result from measurement uncertainty. We choose not to carry out such a procedure, since we feel that the main limitation on the validity of our conclusions is small sample size rather than measurement error. The need for more data on M-class and BFGP asteroids is particularly acute.

6. DISCUSSION

For an asteroid with SC/OC = 0, the echo would likely be due almost entirely to single backscattering from surface elements that are smooth at scales near the wavelength. In such cases we can write $\hat{\sigma}_{\rm OC} = gR$, where R is the power reflection coefficient at normal incidence (or simply the reflectivity) and g is the backscatter gain, which would be unity for a smooth sphere, that is, an isotropic scatterer. For a (near) sphere with surface facets having adirectional rms slope s_0, g would be of order $1 + s_0^2/2$, which for expected slope distributions does not exceed unity by more than a few tens of percent; see, for example, the results of Mitchell *et al.* (1996) for 1 Ceres and 2 Pallas. For our generally nonspherical targets, we expect that the rotation-phase averaging of the echoes leads to values of g that are comparable to but slightly larger than unity.

For targets with nonzero $\mu_{\rm C}$, some of the echo power is due to single scattering from rough surfaces or irregularly shaped objects, or to multiple scattering. Let us use the term "diffuse" to refer collectively to all of the echo not due to specular reflection from smooth surface elements. If the diffuse echo is characterized by OC albedo $\hat{\sigma}_{\rm OC,diff}$ and by polarization ratio $\mu_{\rm C,diff}$, then we can write

$$\hat{\sigma}_{\rm OC,diff} = \frac{\hat{\sigma}_{\rm SC}}{\mu_{\rm C,diff}} = \frac{\mu_{\rm C}\hat{\sigma}_{\rm OC}}{\mu_{\rm C,diff}}, \tag{12}$$

so the part of the OC albedo due to specular reflection from smooth surface elements is

$$\hat{\sigma}_{\rm OC,spec} = \hat{\sigma}_{\rm OC} - \hat{\sigma}_{\rm OC,diff} = \hat{\sigma}_{\rm OC}\left(1 - \frac{\mu_{\rm C}}{\mu_{\rm C,diff}}\right). \tag{13}$$

Analyses based on disk-resolved echoes from the Moon and inner planets (Harmon and Ostro 1985 and references therein) and on empirical and theoretical information about the polarization ratios for diffuse scattering processes (e.g., Cuzzi and Pollack 1978 and references therein) suggest that a reasonable guess for $\mu_{\rm C,diff}$ is in the realm of 0.5. We adopt $\mu_{\rm C,diff} = 0.50 \pm 0.15$; the two-sigma interval 0.20–0.80 covers most measured values tabulated by Harmon and Ostro. For purposes of discussion, we list in the second column of Table IX the corresponding mean value of $\hat{\sigma}_{\rm OC,spec}$ for each taxonomic class. In the same spirit, let us take g to be 1.2 ± 0.1; this is the gain of a (near) sphere with an rms slope of about 32° (two-sigma interval 0°–50°).

For relevant rocks and minerals, it is reasonable to treat R as a function of near-surface bulk density $d_{\rm bulk}$, so we will infer $d_{\rm bulk}$ from R using the empirical relationship presented by Garvin *et al.* (1985):

$$d_{\rm bulk}(R) = 3.2 \ln\left(\frac{1+\sqrt{R}}{1-\sqrt{R}}\right). \tag{14}$$

Equation 14 agrees well with other empirically derived formulae (e.g., Ostro *et al.* 1985) and should be valid to within 10%. Table IX lists near-surface bulk densities corresponding to $R = \hat{\sigma}_{\rm OC,spec}/g$, as well as solid rock densities $d_{\rm solid}$ corresponding to a porosity, $p = 0.5$, which is a typical value for the upper 30 cm of the lunar regolith (Heiken *et al.* 1991, Table 9.5).

Thus Table IX uses reasonable guesses for $\mu_{\rm C,diff}$, g, and porosity to translate disk-integrated radar properties into solid-rock densities. The uncertainties in these guesses propagate into a systematic uncertainty of about 50% in the numbers listed for $d_{\rm solid}$ (or somewhat higher for the M-class estimate). For comparison, typical meteorite values of $d_{\rm solid}$ (Ostro *et al.* 1991a and references therein) are 7.6 g cm^{-3} for irons, 4.9 g cm^{-3} for stony irons, 3.5 g cm^{-3} for ordinary and enstatite chondrites, and 2.7 g cm^{-3} for carbonaceous chondrites (which range from 2.2 g cm^{-3} for CI to 3.4 g cm^{-3} for CO/CV). Given the canonical plausible associations of asteroid classes with meteorite types (Bell *et al.* 1989 and references therein; Gaffey *et al.* 1989), the entries for $d_{\rm solid}$ in Table IX seem reasonable for the S and M classes but high for the C and BFGP classes. Perhaps many members of the last two classes have lower porosity regoliths.

Estimates of the *volume-averaged* bulk densities of the G asteroid 1 Ceres and the B asteroid 2 Pallas (2.1 ± 0.1 g cm^{-3} and 2.6 ± 0.5 g cm^{-3}, respectively; see discussion by Mitchell *et al.* 1996 and references therein) are larger than that for the C asteroid 253 Mathilde (1.3 ± 0.2 g cm^{-3}; Yeomans *et al.* 1997), which is comparable to that estimated for C asteroids from their effects on the orbit of Mars (E. M. Standish, personal communication; see Yeomans *et al.* 1997). Our C and BFGP values of $d_{\rm bulk}$ are in the middle of this suite of nonradar density estimates. The most reliable S-class estimate of volume-averaged bulk density, 2.6 ± 0.5 g cm^{-3} for 243 Ida (Belton *et al.* 1995), is on the high side of the "error" interval in Table IX.

Now let us comment on possible implications of the statistical results from the previous section:

1. *The polarization-ratio distributions of the C, S, BFGP, and M classes are broad.* Within each taxonomic class, MBAs exhibit significant target-to-target variations in near-surface roughness. (Note, however, that the distribution of near-Earth asteroid polarization ratios is about three times broader than the MBA distribution.)

2. *The radar albedo distributions of the C, S, BFGP, and M classes are broad.* The OC albedos of the Moon, Mercury, Venus, and Mars span the narrow range 0.06 to 0.11 (Ostro 1993, Table 2); even the C- and S-class $\hat{\sigma}_{\rm OC}$ distributions are broad by comparison. Near-surface bulk density—and hence solid-rock density, metal fraction, and/or porosity—varies dramatically among mainbelt asteroids and even among MBAs of a given taxonomic class.

3. *There is no reliable evidence that the C, S, BFGP, and M classes have different polarization-ratio distributions.* Despite the likely compositional distinctions between classes, we find no evidence that the degree of centimeter-to-decimeter-scale roughness depends on class.

TABLE VIII
Probabilities Derived from Interclass Comparisons[a]

Variable	Shapiro–Wilk		Levene	Kruskal–Wallis	Dunn			ANOVA	Newman–Keuls			Tukey			Scheffé		
	BFGP C	S M			M-BFGP S-BFGP	M-C S-C	M-S C-BFGP		M-BFGP S-BFGP	M-C S-C	M-S C-BFGP	M-BFGP S-BFGP	M-C S-C	M-S C-BFGP	M-BFGP S-BFGP	M-C S-C	M-S C-BFGP
$\hat{\sigma}_{OC}$	0.013	0.21	0.077	0.0013	0.0006	0.31	0.12	—	—	—	—	—	—	—	—	—	—
	0.24	0.64			0.14	>0.99	0.24		—	—	—	—	—	—	—	—	—
$\ln(\hat{\sigma}_{OC}+0.05)$	0.13	0.42	0.64	0.0013	0.0006	0.31	0.12	0.0001	≤0.01	≤0.01	≤0.01	≤0.01	≤0.05	≤0.01	0.0001	0.039	0.012
	0.39	0.92			0.14	>0.99	0.24		≤0.01	>0.05	≤0.05	≤0.05	>0.05	≤0.05	0.039	>0.99	0.079
$\hat{\sigma}_{TC}$	0.0069	0.12	0.073	0.0022	0.0012	0.26	0.23	—	—	—	—	—	—	—	—	—	—
	0.13	0.76			0.087	>0.99	0.35		—	—	—	—	—	—	—	—	—
$\ln \hat{\sigma}_{TC}$	0.13	0.24	0.41	0.0022	0.0012	0.26	0.23	0.0001	≤0.01	≤0.05	≤0.01	≤0.01	≤0.05	≤0.05	0.0001	0.075	0.048
	0.24	0.79			0.087	>0.99	0.35		≤0.01	>0.05	≤0.01	≤0.01	>0.05	≤0.05	0.0054	>0.99	0.026
$\hat{\sigma}_{OC}-\hat{\sigma}_{SC}$	0.012	0.67	0.014	—	—	—	—	—	—	—	—	—	—	—	—	—	—
	0.74	0.40			—	—	—		—	—	—	—	—	—	—	—	—
$\ln(\hat{\sigma}_{OC}-\hat{\sigma}_{SC}+0.05)$	0.19	0.96	0.35	0.0078	0.0054	0.80	0.23	0.0017	≤0.01	≤0.05	≤0.05	≤0.01	>0.05	≤0.05	0.0019	0.14	0.041
	0.88	0.65			0.34	>0.99	0.22		>0.05	>0.05	>0.05	>0.05	>0.05	>0.05	0.25	0.98	0.22
$\hat{\sigma}_{OC}-2\hat{\sigma}_{SC}$	0.0043	0.40	0.0054	—	—	—	—	—	—	—	—	—	—	—	—	—	—
	0.91	0.20			—	—	—		—	—	—	—	—	—	—	—	—
$\ln(\hat{\sigma}_{OC}-2\hat{\sigma}_{SC}+0.05)$	0.086	0.73	0.14	0.051	0.067	>0.99	0.46	0.031	≤0.05	>0.05	≤0.05	≤0.05	>0.05	>0.05	0.038	0.39	0.11
	0.88	0.48			>0.99	>0.99	0.30		>0.05	>0.05	>0.05	>0.05	>0.05	>0.05	0.83	0.90	0.54
$\hat{\sigma}_{OC}-3\hat{\sigma}_{SC}$	0.0050	0.35	0.0019	—	—	—	—	—	—	—	—	—	—	—	—	—	—
	0.87	0.092			—	—	—		—	—	—	—	—	—	—	—	—
$\ln(\hat{\sigma}_{OC}-3\hat{\sigma}_{SC}+0.05)$	0.070	0.76	0.030	—	—	—	—	—	—	—	—	—	—	—	—	—	—
	0.82	0.31			—	—	—		—	—	—	—	—	—	—	—	—
μ_C	0.18	0.38	0.068	0.16	0.80	>0.99	>0.99	—	—	—	—	—	—	—	—	—	—
	0.042	0.12			0.19	>0.99	>0.99		—	—	—	—	—	—	—	—	—
$\sqrt{\mu}_C$	0.59	0.020	0.33	0.16	0.80	>0.99	>0.99	—	—	—	—	—	—	—	—	—	—
	0.0006	0.027			0.19	>0.99	>0.99		—	—	—	—	—	—	—	—	—

[a] For each variable, eight statistical tests have been performed on our four single-class MBA samples. Each of these procedures tests a particular assumption about how this variable is distributed for the four parent MBA populations. The number listed in the table is the probability that this default assumption—the null hypothesis H_0—is valid. Small probabilities indicate that H_0 is unlikely to be valid, and hence that an alternative hypothesis H_A is favored. H_A generally involves parent distributions which differ from each other or from a particular theoretical distribution. The null and alternative hypotheses for our tests are listed below:

Shapiro–Wilk:

H_0: The parent population for this taxonomic class has a normal distribution in this variable.

H_A: The parent population for this taxonomic class does not have a normal distribution in this variable.

Levene's test:

H_0: The four single-class parent populations have equal variance in this variable.

H_A: At least two of the four single-class parent populations have different variances in this variable.

Kruskal–Wallis test:

H_0: The four single-class parent populations have identical distributions in this variable.

H_A: The four single-class parent populations have identical distributions in this variable, except that at least two of the four medians differ from each other.

Dunn's *post hoc* test (performed after the Kruskal-Wallis test):

H_0: The two single-class parent populations being considered have identical distributions in this variable.

H_A: The two single-class parent populations being considered have identical distributions in this variable, except that the medians differ from each other.

One-way unblocked analysis of variance (ANOVA):

H_0: The four single-class parent populations have identical normal distributions in this variable.

H_A: The four single-class parent populations have identical normal distributions in this variable, except that at least two of the four means differ from each other.

Newman–Keuls, Tukey "honestly significant difference," and Scheffé *post hoc* tests (performed after ANOVA):

H_0: The two single-class parent populations being considered have identical normal distributions in this variable.

H_A: The two single-class parent populations being considered have identical normal distributions in this variable, except that the means differ from each other.

TABLE IX
MBA Near-Surface Densities by Taxonomic Class

Class	$\hat{\sigma}_{OC,spec} = \hat{\sigma}_{OC}(1-\mu_C/\mu_{C,diff})$	$R = \hat{\sigma}_{OC,spec}/g$	d_{bulk} (g cm^{-3})	d_{solid} for $p=0.5$ (g cm^{-3})
BFGP	0.079 ± 0.056	0.066 ± 0.048	1.7 ± 0.7	3.4 ± 1.4
C	0.112 ± 0.058	0.093 ± 0.050	2.0 ± 0.6	4.0 ± 1.2
S	0.100 ± 0.075	0.083 ± 0.064	1.9 ± 0.9	3.8 ± 1.8
M	0.213 ± 0.182	0.178 ± 0.154	2.9 ± 1.7	5.8 ± 3.4

Note. For each taxonomic class, the listed standard deviation for $\hat{\sigma}_{OC,spec}$ is the sum in quadrature of the standard deviation of the individual-target best estimates and the mean of the individual-target standard deviations. Standard deviations for $\hat{\sigma}_{OC,spec}$ are then propagated into those listed in the last three columns. Uncertainties in the reasonable guesses made for $\mu_{C,diff}$, g, and porosity (see text) propagate into a systematic uncertainty of about 50% in the numbers listed for solid-rock density d_{solid} (or somewhat higher for the M-class estimate).

4. *There is good reason to believe that M asteroids tend to have higher albedos and a wider range of albedos than do the C, S, and BFGP classes.* The radar-brightest M asteroids are likely to be iron-meteorite analogues. The radar-darkest members of this class likely have lower surface metal concentrations.

5. *For the M class, radar albedo is anticorrelated with visual albedo.* Visual albedo may offer a criterion for splitting the M class into relatively metal-rich and metal-poor subclasses.

6. *There is no reason to believe that the C and S classes have different radar albedo distributions.* If the *only* difference between S and C asteroids were their solid-rock density d_{solid}, then, if forced to choose between stony irons and ordinary chondrites as the S-class meteorite analogue, we would have to favor ordinary chondrites, because their solid-rock densities are less removed from those of carbonaceous chondrites. On the other hand, high-porosity stony-iron analogues and low-porosity ordinary-chondrite analogues could have identical near-surface bulk densities and therefore identical radar reflectivities.

7. *There is an indication that BFGP asteroids are radar-darker than our other sampled classes.* These objects are likely candidates for being mineralogically similar to the lowest-d_{solid} meteorites (CI and CM chondrites).

In terms of the size of the MBA radar sample, radar observations are where UBV photometry stood three decades ago (Chapman and Zellner 1978). However, the upgrading of the Arecibo Observatory has doubled that telescope's range, extending it roughly from the main belt's inner edge to its outer edge. Hundreds of MBAs are now detectable at single-date SNRs much larger than those achieved in the observations reported here (Ostro 1993, Fig. 29).

Obviously it is desirable to perform a thorough survey of MBA radar properties. Since SNR increases as the square root of the integration time, there are many objects for which a week or two of daily observations could yield dataset SNRs of at least several hundred. This minimum is large enough for delay-Doppler imaging to permit the construction of accurate models of target shape and backscatter gain (Hudson 1993), and hence of radar reflectivity and near-surface bulk density.

TABLE X
Polarization Ratios Obtained for 7 Iris

Year	OC SNR	λ (cm)	δ_{rad} (°)	μ_C
1980	22	13	-69 ± 10	0.08 ± 0.03
1984	28	13	-21 ± 8	0.19 ± 0.03
1991	19	3.5	-56 ± 10	0.19 ± 0.05
1995	60	3.5	-34 ± 8	0.33 ± 0.04

APPENDIX

Comments on Individual Objects

7 Iris

Mitchell *et al.* (1995) analyze monostatic data obtained at Arecibo in 1980 and 1984 and at Goldstone in 1991. They note that the polarization ratios obtained for these three experiments are significantly different from each other, suggesting "the possibility of either regional or scale-dependent variations in small-scale structure."

Iris was observed again from Goldstone in 1995 (Fig. 1), yielding a particularly large μ_C value. The results to date (Table X) are consistent with the hypothesis that views at lower latitudes and shorter observing wavelengths yield higher polarization ratios.

18 Melpomene (see Section 4)

21 Lutetia (see Section 4)

27 Euterpe

Euterpe was not observed by IRAS, but Dunham (1997) fits an elliptical profile to 1993 occultation data. The nine observed chords yield an ellipse whose major and minor axes are 124.2 ± 1.7 km and 75.2 ± 1.3 km (D. Dunham, personal communication). The major axis is close to the TRIAD value of 118 km (Bowell *et al.* 1979, Morrison 1974), but the high degree of flattening is surprising, given a maximum lightcurve amplitude of only 0.15 mag (Lagerkvist *et al.* 1989).

These data can be reconciled if we model Euterpe as a triaxial ellipsoid viewed with the line of sight roughly parallel to the intermediate-valued principal axis during the occultation. The measured maximum value of Δm yields the rough estimate $a/b = 1.15 \pm 0.15$. This value, together with the occultation ellipse, imply that $b/c = 1.43 \pm 0.20$ (note, however, that the observed chords do not densely cover the profile). Hence we adopt the "safe" value $b/c = 1.3 \pm 0.3$, covering possibilities from a prolate spheroid to the shape implied by the occultation fit. With these axis ratios we expect $2c$ to be approximately (1.43/1.3) times 75 km, or 83 km. If the infrared observations were made pole-on, we would have $D_{IR} = 2\sqrt{ab}$; our adopted axis ratios would then imply principal axis diameters of $127 \times 110 \times 85$ km. This value of $2c$ is roughly what we were expecting, whereas IR observations away from the pole would yield larger dimensions. We therefore adopt these lengths for our reference ellipsoid.

41 Daphne

Daphne was observed for six days in 1985. Three of these days were devoted to dual-circular polarization measurements, while the other three were used to obtain dual-linear polarization data. The results of both experiments are shown in Table XI.

If Daphne's surface is smooth at scales within an order of magnitude of the observing wavelength (13 cm), we expect the received echoes to have (a) low values of both μ_C and μ_L, and (b) σ_{OC} roughly equal to σ_{SL}. The OC and SL

TABLE XI
Dual-Circular vs Dual-Linear Data for 41 Daphne

Pol.	SNR	$\hat{B}_{eq}$ (Hz)	$\hat{B}_{ZC}$ (Hz)	σ_{pol} (km^2)	$\hat{\sigma}_{pol}$	μ
OC, SC	11	500 ± 20	560 ± 20	2900 ± 770	0.11 ± 0.04	0.13 ± 0.08
SL, OL	12	570 ± 30	850 ± 30	3300 ± 840	0.12 ± 0.04	0.26 ± 0.08

cross sections listed in Table XI are indeed equal to within the stated errors. Although μ_L is somewhat higher than μ_C, this conflict is an illusion, since feed rotation during the 18-min echo time delay biases μ_L upward.

We find that bandwidth estimates $\hat{B}_{eq}$ and (especially) $\hat{B}_{ZC}$ are larger for the SL than for the OC echo, for all combinations of folding and frequency smoothing (see Table XI). (Note that these two data sets represent similar rotation phase coverage.) Since the cross sections agree well, as discussed earlier, and since the SNR is only about 12 for each of these two spectral sums, we are not concerned about this apparent discrepancy. To take it (partially) into account, we restrict our estimate of B to be at least as large as the smaller (OC) value: $B \geq 540$ Hz.

84 Klio

Klio's rotation period and shape are not well constrained by published lightcurves. Zeigler and Wampole (1988) obtain a period of 5.80 ± 0.02 h based on three nights of observations in October 1985. Their composite lightcurve has an amplitude of only 0.06 ± 0.01 mag, and has three maxima and minima per reported rotational cycle. On the other hand, the single lightcurve published by Weidenschilling *et al.* (1990) was obtained only one week later, but is at best "marginally compatible" with the results of Zeigler and Wampole. Unless two data points taken at high air mass are rejected, the Weidenschilling *et al.* lightcurve implies a period significantly longer than 6 h.

Because photometry of Klio is restricted to just one longitude, we cannot decide whether the low lightcurve amplitude results from a nearly spherical shape or from nearly pole-on viewing. Our *a priori* model is a sphere whose diameter is within 25% of D_{IR}. The predicted 13-cm $B_{max}(\delta_{rad} = 0)$ is equal to 2190 ± 590 Hz divided by the rotation period in hours. Future photometry could greatly reduce the errors on the model's parameters.

The summed OC signal for Klio lets us place only a lower limit on the bandwidth: $B \geq 105$ Hz. Since $B_{max}(\delta_{rad} = 0) \geq B$, this limit on B is also a lower limit on $B_{max}(\delta_{rad} = 0)$. Given the assumption that $B_{max}(\delta_{rad} = 0) = 4\pi D/\lambda P$, we obtain the inequality $P \leq 4\pi D/\lambda B$, implying that $P \leq 32$ h at the 95% confidence level.

105 Artemis

No pole determination has been published for Artemis and the rotation period is uncertain. Schober *et al.* (1994) estimate that $P = 16.84 \pm 0.01$ h, but the composite lightcurve they present appears to have much greater scatter than their stated precision would indicate. We adopt this period estimate but assign a 3-h standard error. An incorrect value for the period would primarily influence our radar-based pole constraints; the quality of the radar phase coverage would be poor for *any* long rotation period.

TABLE XII
Radar Data for 105 Artemis on Two Different Dates

Date	SNR	$\hat{B}_{eq}$ (Hz)	$\hat{B}_{ZC}$ (Hz)	σ_{OC} (km^2)[a]	μ_C
1988 Jun 10	20	58 ± 5	130 ± 30	1790 ± 86	0.22 ± 0.05
1988 Jun 11	20	52 ± 5	120 ± 20	1720 ± 83	0.06 ± 0.05

[a] Stated standard errors on σ_{OC} reflect the contributions of receiver noise but not calibration uncertainties, as appropriate for date-to-date comparisons.

Some of the data obtained during the 1988 radar experiment were delay measurements obtained for astrometric purposes (Ostro *et al.* 1991b). The cw data indicate possible variation in μ_C across the surface. These data cover two rotation phase intervals, one for each of the two days of observations. Summed spectra from each of these two days yield statistically identical OC cross sections (Table XII), but polarization ratios which differ by slightly over two standard deviations: 0.22 ± 0.05 vs 0.06 ± 0.05. Observations with the upgraded Arecibo radar facility should easily reveal whether or not this difference is real.

139 Juewa

Juewa's rotation period is twofold ambiguous, with either 20.9 or 41.8 h permitted by the photometric data. Michałowski (1993) has published the only pole determination for this object; he states that 20.91 h is the most probable sidereal period, but notes that this value "may be completely wrong." Hence we consider the implications of both of these candidate periods for obtaining radar-based pole constraints.

Michałowski obtains a single pole solution at $\lambda = 117^\circ \pm 14^\circ$, $\beta = +50^\circ \pm 12^\circ$. The corresponding axis ratios for a model ellipsoid are $a/b = 1.21 \pm 0.20$ and $b/c = 1.68 \pm 0.45$. This solution has not been confirmed by independent studies, and it does not yield an unambiguous sidereal period and rotation sense. Therefore we will increase Michałowski's stated errors on the pole direction. We assume that the pole lies within a 25° radius of $(\lambda, \beta) = (117^\circ, +50^\circ)$ and that the axis ratios are $a/b = 1.2 \pm 0.2$ and $b/c = 1.7 \pm 0.5$. (The published uncertainties on the axis ratios are fairly large, so we have chosen not to increase them significantly.)

324 Bamberga

Bamberga is discussed by de Pater *et al.* (1994), who consider monostatic data from Arecibo and Goldstone along with bistatic Goldstone-VLA measurements. Here we consider only the monostatic spectra, largely in order to give separate tabular summaries of the 13- and 3.5-cm data. There is only one minor revision to note. The latest IRAS estimate of Bamberga's diameter is 229 ± 7 km (Ted97); this value is 5% smaller than the older IRAS value of 242 ± 7 km used by de Pater *et al.*, but agrees with the occultation diameter estimate of 228 ± 2 km (Millis *et al.* 1989). This downward revision of D_{IR} results in radar albedo estimates 10% higher than those of de Pater *et al.*

Bamberga has a maximum lightcurve amplitude of 0.05 mag (Lagerkvist *et al.* 1996), which implies that our reference ellipsoid has a maximum breadth $2a$ nearly as large as the 242 km value used by de Pater *et al.* for their model sphere. Thus, the predicted 13- and 3.5-cm $B_{max}(\delta_{rad} = 0)$ values—and hence the pole constraints—are essentially unchanged from that paper.

393 Lampetia (see Section 4)

532 Herculina

Our Herculina data are weak. Moreover, data taken on different dates for the same rotation phase interval give highly discrepant OC cross sections. Observations of 2 Pallas made on these dates had unusually low SNR relative to data taken at two other oppositions (Mitchell *et al.* 1996), so we believe that system problems were responsible for Herculina's strong σ_{OC} variations. We analyze the weighted sum of spectra taken on the four observing dates, but assign a 50% error to our cross sections.

ACKNOWLEDGMENTS

We thank the Goldstone and Arecibo technical staffs for their assistance. C.M. greatly benefitted from a NASA-ASEE 1997 Summer Faculty Fellowship in Aeronautics and Space Research. He also thanks Lance Benner for technical aid and helpful discussions during his stay at JPL, and Al Harris for information on several lightcurves. The Arecibo Observatory is part of the National Astronomy and Ionosphere Center, which is operated by Cornell University under a cooperative agreement with the National Science Foundation and with support from the National Aeronautics and Space Administration (NASA). Part of this

research was conducted at the Jet Propulsion Laboratory, California Institute of Technology, under contract with NASA. Work at the Center for Astrophysics was supported in part by NASA and by the Smithsonian Institution.

REFERENCES

Bell, J. F., D. R. Davis, W. K. Hartmann, and M. J. Gaffey 1989. Asteroids: The big picture. In *Asteroids II* (R. P. Binzel, T. Gehrels, and M. S. Matthews, Eds.), pp. 921–945. Univ. of Arizona Press, Tucson.

Belskaya, I. N., and C.-I. Lagerkvist 1996. Physical properties of M class asteroids. *Planet. Space Sci.* **44**, 783–794.

Belton, M. J. S., and 16 colleagues 1995. Bulk density of Asteroid 243 Ida from the orbit of its satellite Dactyl. *Nature* **374**, 785–788.

Birlan, M., M. Fulchignoni, and M. A. Barucci 1996. Effects of IRAS albedo correction on the G-mode asteroid taxonomy. *Icarus* **124**, 352–354.

Bowell, E., T. Gehrels, and B. Zellner 1979. Magnitudes, colors, types and adopted diameters of the asteroids. In *Asteroids* (T. Gehrels, Ed.), pp. 1108–1129. Univ. of Arizona Press, Tucson.

Brown, R. H. 1985. Ellipsoidal geometry in asteroid thermal models: The standard radiometric model. *Icarus* **64**, 53–63.

Chapman, C. R., and B. Zellner 1978. The role of Earth-based observations of asteroids during the next decade. In *Asteroids: An Exploration Assessment* (D. Morrison and W. C. Wells, Eds.), pp. 183–191. [NASA Conf. Pub. 2053]

Conover, W. J. 1980. *Practical Nonparametric Statistics*, 2nd ed. Wiley, New York.

Cuzzi, J. N., and J. B. Pollack 1978. Saturn's rings: Particle composition and size distribution as constrained by microwave observations. I. Radar observations. *Icarus* **33**, 233–262.

Daniel, W. W. 1990. *Applied Nonparametric Statistics*, 2nd ed. PWS-Kent, Boston.

De Angelis, G. 1995. Asteroid spin, pole and shape determinations. *Planet. Space Sci.* **43**, 649–682.

de Pater, I., P. Palmer, D. L. Mitchell, S. J. Ostro, D. K. Yeomans, and L. E. Snyder 1994. Radar aperture synthesis observations of asteroids. *Icarus* **111**, 489–502.

Dollfus, A., M. Wolff, J. E. Geake, D. F. Lupishko, and L. M. Dougherty 1989. Photopolarimetry of asteroids. In *Asteroids II* (R. P. Binzel, T. Gehrels, and M. S. Matthews, Eds.), pp. 594–616. Univ. of Arizona Press, Tucson.

Dotto, E., M. A. Barucci, M. Fulchignoni, M. Di Martino, A. Rotundi, R. Burchi, and A. Di Paolantonio 1992. M-type asteroids: Rotational properties of 16 objects. *Astron. Astrophys. Suppl. Ser.* **95**, 195–211.

Dunham, D. W. 1997. Recent results from asteroidal occultations. *Occultation Newslett.* **6**, 300–303.

Efron, B., and R. J. Tibshirani 1993. *An Introduction to the Bootstrap*. Chapman and Hall, New York.

Gaffey, M. J., J. F. Bell, and D. P. Cruikshank 1989. Reflectance spectroscopy and asteroid surface mineralogy. In *Asteroids II* (R. P. Binzel, T. Gehrels, and M. S. Matthews, Eds.), pp. 98–127. Univ. of Arizona Press, Tucson.

Garvin, J. B., J. W. Head, G. H. Pettengill, and S. H. Zisk 1985. Venus global radar reflectivity and correlations with elevation. *J. Geophys. Res.* **90**, 6859–6871.

Gehrels, T. 1970. Photometry of asteroids. In *Surfaces and Interiors of Planets and Satellites* (A. Dollfus, Ed.), pp. 319–376. Academic Press, London.

Harmon, J. K., and S. J. Ostro 1985. Mars: Dual-polarization radar observations with extended coverage. *Icarus* **62**, 110–128.

Harris, A. W., and J. W. Young 1989. Asteroid lightcurve observations from 1979–1981. *Icarus* **81**, 314–364.

Heiken, G. H., D. T. Vaniman, and B. M. French 1991. *Lunar Sourcebook*. Cambridge Univ. Press, New York.

Hoffmann, M., and E. H. Geyer 1990. A photometric study of 18 Melpomene. In *Asteroids, Comets, Meteors III* (C.-I. Lagerkvist, H. Rickman, B. A. Lindblad, and M. Lindgren, Eds.), pp. 111–114. Uppsala University.

Howell, E. S., E. Merényi, and L. A. Lebofsky 1994. Classification of asteroid spectra using a neural network. *J. Geophys. Res.* **99**, 10,847–10,865.

Hudson, R. S. 1993. Three-dimensional reconstruction of asteroids from radar observations. *Remote Sens. Rev.* **8**, 195–203.

Jurgens, R. F. 1982. Radar backscattering from a rough rotating triaxial ellipsoid with applications to the geodesy of small asteroids. *Icarus* **49**, 97–108.

Kell, R. E., and R. A. Ross 1970. Radar cross section of targets. In *Radar Handbook* (M. I. Skolnik, Ed.), Chap. 27. McGraw–Hill, New York.

Lagerkvist, C.-I., A. Erikson, H. Debehogne, L. Festin, P. Magnusson, S. Mottola, T. Oja, G. De Angelis, I. N. Belskaya, M. Dahlgren, M. Gonano-Beurer, J. Lagerros, K. Lumme, and S. Pohjolainen 1995. Physical studies of asteroids. XXIX. Photometry and analysis of 27 asteroids. *Astron. Astrophys. Suppl. Ser.* **113**, 115–129.

Lagerkvist, C.-I., A. W. Harris, and V. Zappalà 1989. Asteroid lightcurve parameters. In *Asteroids II* (R. P. Binzel, T. Gehrels, and M. S. Matthews, Eds.), pp. 1162–1179. Univ. of Arizona Press, Tucson.

Lagerkvist, C.-I., P. Magnusson, I. Belskaya, J. Piironen, J. Warell, and M. Dahlgren 1996. *Asteroid Photometric Catalogue*, Fourth Update. Uppsala. Astron. Obs.

Lebofsky, L. A., and J. R. Spencer 1989. Radiometry and thermal modeling of asteroids. In *Asteroids II* (R. P. Binzel, T. Gehrels, and M. S. Matthews, Eds.), pp. 128–147. Univ. of Arizona Press, Tucson.

Lupishko, D. F., and F. P. Velichko 1987. Sense of rotation for Asteroids 21, 63, 216, and 349. *Kinem. Phys. Celest. Bodies* **3**, 57–65.

Lupishko, D. F., F. P. Velichko, I. N. Belskaya, and V. G. Shevchenko 1987. Pole coordinates and phase dependence of the light of the Asteroid 21 Lutetia. *Kinem. Phys. Celest. Bodies* **3**, 36–38.

Michałowski, T. 1992. Spin vectors of Asteroids 21 Lutetia, 196 Philomela, 250 Bettina, 337 Devosa and 804 Hispania. In *Asteroids, Comets, Meteors 1991* (A. W. Harris and E. Bowell, Eds.), pp. 417–419. Lunar and Planetary Institute, Houston.

Michałowski, T. 1993. Poles, shapes, senses of rotation, and sidereal periods of asteroids. *Icarus* **106**, 563–572.

Michałowski, T. 1996. Pole and shape determination for 12 Asteroids. *Icarus* **123**, 456–462.

Michałowski, T., F. P. Velichko, M. Di Martino, Yu. N. Krugly, V. G. Kalashnikov, V. G. Shevchenko, P. V. Birch, W. D. Sears, P. Denchev, and T. Kwiatkowski 1995. Models of four asteroids: 17 Thetis, 52 Europa, 532 Herculina, and 704 Interamnia. *Icarus* **118**, 292–301.

Millis, R. L., L. H. Wasserman, O. G. Franz, E. Bowell, R. A. Nye, D. T. Thompson, N. M. White, W. B. Hubbard, R. E. Eplee, Jr., L. A. Lebofsky, R. L. Marcialis, R. J. Greenberg, D. M. Hunten, H. J. Reitsema, Q. Bochen, D. W. Dunham, P. D. Maley, A. R. Klemola, and D. K. Yeomans 1989. Observations of the 8 December 1987 occultation of AG $+40^{\circ}0783$ by 324 Bamberga. *Astron. J.* **98**, 1094–1099.

Mitchell, D. L., R. S. Hudson, S. J. Ostro, and K. D. Rosema 1998. Shape of Asteroid 433 Eros from inversion of Goldstone radar Doppler spectra. *Icarus* **131**, 4–14.

Mitchell, D. L., S. J. Ostro, R. S. Hudson, K. D. Rosema, D. B. Campbell, R. Vélez, J. F. Chandler, I. I. Shapiro, J. D. Giorgini, and D. K. Yeomans 1996. Radar observations of Asteroids 1 Ceres, 2 Pallas, and 4 Vesta. *Icarus* **124**, 113–133.

Mitchell, D. L., S. J. Ostro, K. D. Rosema, R. S. Hudson, D. B. Campbell, J. F. Chandler, and I. I. Shapiro 1995. Radar observations of Asteroids 7 Iris, 9 Metis, 12 Victoria, 216 Kleopatra, and 654 Zelinda. *Icarus* **118**, 105–131.

Morrison, D. 1974. Radiometric diameters and albedos of 40 asteroids. *Astrophys. J.* **194**, 203–212.

Norton, K. A., and A. C. Omberg 1947. The maximum range of a radar set. *Proc. Inst. Radio Eng.* **35**, 4–24.

Ostro, S. J. 1993. Planetary radar astronomy. *Rev. Mod. Phys.* **65**, 1235–1279.

Ostro, S. J. 1998. Planetary radar. In *The Encyclopedia of the Solar System* (T. Johnson, P. Weissman, and L. A. McFadden, Eds.), pp. 773–807. Academic Press, San Diego.

Ostro, S. J., D. B. Campbell, J. F. Chandler, A. A. Hine, R. S. Hudson, K. D. Rosema, and I. I. Shapiro 1991a. Asteroid 1986 DA: Radar evidence for a metallic composition. *Science* **252**, 1399–1404.

Ostro, S. J., D. B. Campbell, J. F. Chandler, I. I. Shapiro, A. A. Hine, R. Vélez, R. F. Jurgens, K. D. Rosema, R. Winkler, and D. K. Yeomans 1991b. Asteroid radar astrometry. *Astron. J.* **102**, 1490–1502.

Ostro, S. J., D. B. Campbell, R. A. Simpson, R. S. Hudson, J. F. Chandler, K. D. Rosema, I. I. Shapiro, E. M. Standish, R. Winkler, D. K. Yeomans, R. Vélez, and R. M. Goldstein 1992. Europa, Ganymede, and Callisto: New radar results from Arecibo and Goldstone. *J. Geophys. Res.* **97**, 18,227-18,244.

Ostro, S. J., D. B. Campbell, and I. I. Shapiro 1983. Radar observations of Asteroid 1685 Toro. *Astron. J.* **88**, 565–576.

Ostro, S. J., D. B. Campbell, and I. I. Shapiro 1985. Mainbelt asteroids: Dual-polarization radar observations. *Science* **229**, 442–446.

Ostro, S. J., K. D. Rosema, and R. F. Jurgens 1990. The shape of Eros. *Icarus* **84**, 334–351.

Rivkin, A. S., E. S. Howell, D. T. Britt, L. A. Lebofsky, M. C. Nolan, and D. D. Branston 1995. Three-micron spectrophotometric survey of M-and E-class asteroids. *Icarus* **117**, 90–100.

Rivkin, A. S., L. A. Lebofsky, D. T. Britt, and E. S. Howell 1997. Three-micron survey of E- and M-class asteroids: Final results. *Bull. Am. Astron. Soc.* **29**, 972–973. [Abstract]

Scaltriti, F., V. Zappalà, and H. J. Schober 1979. The rotations of 128 Nemesis and 393 Lampetia: The longest known periods to date. *Icarus* **37**, 133–141.

Schober, H. J., A. Erikson, G. Hahn, C.-I. Lagerkvist, R. Albrecht, W. Ornig, A. Schroll, and M. Stadler 1994. Physical studies of asteroids. XXVIII. Lightcurves and photoelectric photometry of Asteroids 2, 14, 51, 105, 181, 238, 258, 369, 377, 416, 487, 626, 679, 1048 and 2183. *Astron. Astrophys. Suppl. Ser.* **105**, 281–300.

Snedecor G. W., and W. G. Cochran 1980. *Statistical Methods*, 7th ed. Iowa Univ. Press, Ames, IA.

Tholen, D. J. 1989. Asteroid taxonomic classifications. In *Asteroids II* (R. P. Binzel, T. Gehrels, and M. S. Matthews, Eds.), pp. 1139–1150. Univ. of Arizona Press, Tucson.

Tholen, D. J., and M. A. Barucci 1989. Asteroid taxonomy. In *Asteroids II* (R. P. Binzel, T. Gehrels, and M. S. Matthews, Eds.), pp. 298–315. Univ. of Arizona Press, Tucson.

Tiuri, M. E. 1964. Radio astronomy receivers. *IEEE Trans. Antennas Propag.* **AP-12**, 930–938.

Weidenschilling, S. J., C. R. Chapman, D. R. Davis, R. Greenberg, D. H. Levy, R. P. Binzel, S. M. Vail, M. Magee, and D. Spaute 1990. Photometric geodesy of main-belt asteroids. III. Additional lightcurves. *Icarus* **86**, 402–447.

Yeomans, D. K., and 12 colleagues 1997. Estimating the mass of Asteroid 253 Mathilde from tracking data during the NEAR flyby. *Science* **278**, 2106–2109.

Zappalà, V., M. Di Martino, P. Farinella, and P. Paolicchi 1984. An analytical method for the determination of the rotational direction of asteroids. In *Asteroids, Comets, Meteors* (C.-I. Lagerkvist and H. Rickman, Eds.), pp. 73–76. Uppsala University.

Zar, J. H. 1996. *Biostatistical Analysis*, 3rd ed. Prentice-Hall, Upper Saddle River, NJ.

Zeigler, K. W., and R. C. Wampole 1988. Photoelectric photometry of Asteroids 84 Klio and 678 Fredeguendis. *Minor Planet Bull.* **15**, 15–16.